Journal of Materials Research and Technology 42 (2026) 7563–7584

Contents lists available at ScienceDirect

Journal of Materials Research and Technology

journal homepage: www.elsevier.com/locate/jmrt

Arc distribution as a key driver of inclusion redistribution in Vacuum Arc Remelting (VAR)

Mehran Abdi [a,*], Ebrahim Karimi-Sibaki [a,b], Menghuai Wu [a], Jan Bohacek [c], Abdellah Kharicha [a,**]

[a] Chair for Simulation and Modeling of Metallurgical Processes, Department of Metallurgy, Technical University of Leoben, Franz-Josef Street 18, 8700, Leoben, Austria
[b] Christian Doppler Laboratory for Reactive Flows in Green Steel Production and Refinement, Technical University of Leoben, Franz-Josef Street 18, 8700, Leoben, Austria
[c] Heat Transfer and Fluid Flow Laboratory, Faculty of Mechanical Engineering, Brno University of Technology, Technicka 2896/2, 61669, Brno, Czech Republic

ARTICLE INFO

Keywords:
Vacuum arc remelting (VAR)
Transient ingot growth
Arc distribution
Side arcing
Magnetohydrodynamics (MHD)
Inclusions

ABSTRACT

A transient numerical model is developed to investigate inclusion transport and entrapment during full ingot growth in the Vacuum Arc Remelting (VAR) of the nickel-based superalloy GH4720Li. The model resolves the coupled electromagnetic field, melt-pool flow, solidification, and Lagrangian inclusion motion, enabling a quantitative assessment of arc behavior and inclusion entry conditions. Parametric studies show that increasing side arcing, whereby a portion of the electric current passes through the crown and along the lateral wall of the electrode toward the mold, produces a shallower melt-pool profile, weakens outward inclusion transport, and shifts inclusion entrapment away from the ingot sidewall toward the ingot interior. A constricted arc distribution, which produces a deeper and narrower melt pool, modifies the flow structure and enhances inward-directed transport, thereby reducing peripheral accumulation and promoting a more radially distributed inclusion pattern. Drip-short events, defined as the formation of molten metal bridges between the electrode and the ingot, introduce inclusions at greater depths, leading to a more distributed entrapment pattern throughout the melt pool. Model predictions are validated against experimental observations, providing quantitative guidance for improving ingot cleanliness.

1. Introduction

Vacuum arc remelting (VAR) is a secondary metallurgical process designed to produce ingots with high chemical uniformity and minimal impurities. During VAR, a consumable electrode is gradually melted by a direct current arc within a vacuum chamber. The molten metal droplets detach from the electrode and collect in a water-cooled copper mold, where the balance between arc heating, droplet addition, and mold cooling sustains a stable hemispherical molten pool at the top of the ingot [1] as shown in Fig. 1(a). In industry, VAR is a crucial process for producing critical alloys such as titanium, zirconium, nickel-based alloys, and special steels [2,3]. They serve as critical materials in high-performance industries, including aerospace, energy, defense, and medicine [4]. The vacuum environment in VAR minimizes oxidation, leading to the production of a high-purity material with exceptional cleanliness [5], homogeneity [6], and superior mechanical properties [7], including enhanced fatigue and fracture toughness [8].

The VAR process facilitates the removal of low-density oxide inclusions and promotes the evaporation of high-vapor-pressure impurities such as Pb, Sn, Bi, and Mn. Despite these refining mechanisms, inclusions remain a major challenge in VAR due to their detrimental effects on mechanical properties, fatigue resistance, and overall ingot integrity [9,10]. Inclusions in VAR can be broadly categorized either by their chemical composition, such as oxides (e.g., Al_2O_3, MgO) [11,12], nitrides (e.g., TiN, ZrN) [13], carbides (e.g., NbC, TiC) [14], carbonitrides (e.g., Ti(C,N)) [15], sulfides (e.g., MnS, CaS) [16], and composite inclusions combining multiple phases [17], or by their origin, as either endogenous (formed within the melt during solidification or reaction) or exogenous (introduced from external sources like electrode machining, refractory erosion, or crown fall-in) [18–21]. In the high-temperature VAR environment, inclusions can either remain dissolved in the melt 12,13,22–24 or precipitate [19,25] depending on local thermodynamic

* Corresponding author.
** Corresponding author.
E-mail addresses: mehran.abdi@unileoben.ac.at (M. Abdi), abdellah.kharicha@unileoben.ac.at (A. Kharicha).

https://doi.org/10.1016/j.jmrt.2026.04.262
Received 27 February 2026; Received in revised form 22 April 2026; Accepted 30 April 2026
Available online 2 May 2026

and kinetic conditions [19].

The behavior and final distribution of the remaining inclusions in the molten pool and finally in the ingot, however, are governed by several parameters, most notably the arc distribution in the vacuum region and the electric current distribution through the ingot [26,27], which will be discussed in the following.

The electric arc is sustained by cathode spots 28–31, which act as localized initiation sites for arc discharge. [32–34]. The initiation of these spots is sensitive to local surface conditions, and impurities, oxides, or inclusions may locally enhance electron emission and thereby facilitate spot ignition, which may locally increase temperature and promote evaporation of volatile impurity species [35]. In VAR, the arc established between the electrode tip (cathode) and the ingot top (anode) delivers the thermal energy necessary for electrode remelting. The stability and distribution of cathode spots are critical, as they govern arc behavior in the vacuum region [32,36]. Depending on the cathode spot pattern [33,37], the arc may appear in diffuse, diffuse columnar, or multiple modes [33,38,39], each generating distinct thermal gradients and flow patterns in the molten pool and ultimately influencing inclusion distribution.

Electrical current originates at the electrode tip and splits into two paths: one enters the ingot directly, while the other bypasses the melt pool through the crown and mold as side arcing (accounts for 15–70% of the total current) [40–42]. As solidification proceeds, shrinkage reduces ingot–mold contact [43], creating an interfacial resistance that forces the current to flow downward toward the base plate before entering the mold.

The VAR process lessens the inclusion through several mechanisms: stable arc operation ensures uniform melting and reduces spatter or unmelted electrode fall-in Refs. [6,44–46]; the electromagnetic stirring and thermal convection within the molten pool promote inclusion floatation to the pool surface or rejection to the ingot outside edge [47,48]; and directional solidification from the base upward helps push inclusions ahead of the solid–liquid interface, reducing their entrapment [49,50]. Also, the high vacuum environment facilitates the evaporation or dissociation of volatile impurities and gaseous reaction products [11,51]. Process parameters such as melt current, arc gap, and vacuum level are carefully optimized to enhance these effects, while high-quality, inclusion-minimized electrodes are used to prevent exogenous contamination [52–54]. Despite its effectiveness, VAR cannot yet produce truly inclusion-free alloys [15,55,56].

Measuring inclusions in VAR ingots is inherently challenging due to their microscopic size, complex spatial distribution, and the limitations of available detection techniques. For instance, Zhang et al. [57] identified more than twenty different characterization methods (such as MMO, LAMMS, SAM, X-rays, etc.) for non-metallic inclusions alone, each with specific advantages and disadvantages, underscoring the difficulty of achieving a comprehensive and representative assessment. This methodological diversity illustrates how obtaining statistically reliable data for large ingots remains a major challenge, ultimately complicating both representative sampling and thorough experimental characterization [58].

On the other hand, simulation studies have significantly advanced the understanding of inclusion behavior in VAR. Using CFD–particle tracking, Zhang et al. [59] showed that shelf fragments larger than 10 mm can survive and form white-spot defects [19,60–62], whereas smaller fragments dissolve. They later developed a dendrite-cluster fall-in model that identified particle size, composition, and thermal state as the key parameters controlling dissolution versus defect formation [45].

Ghazal et al. [22] modeled hard-α defects in Ti alloys, demonstrating that dissolution strongly depends on pool thermohydrodynamics. For GH4169 alloy in VAR, Jiang et al. [63] found that large inclusions (~50 μm) migrate outward to the ingot edge while smaller ones (2–10 μm) remain suspended and risk interior entrapment, with transport controlled by electromagnetic flow and thermal–buoyant flow. In a related study, Jiang et al. [52] showed that small inclusions (2–10 μm) follow bulk flow, large ones (20–50 μm) float to the surface, and medium

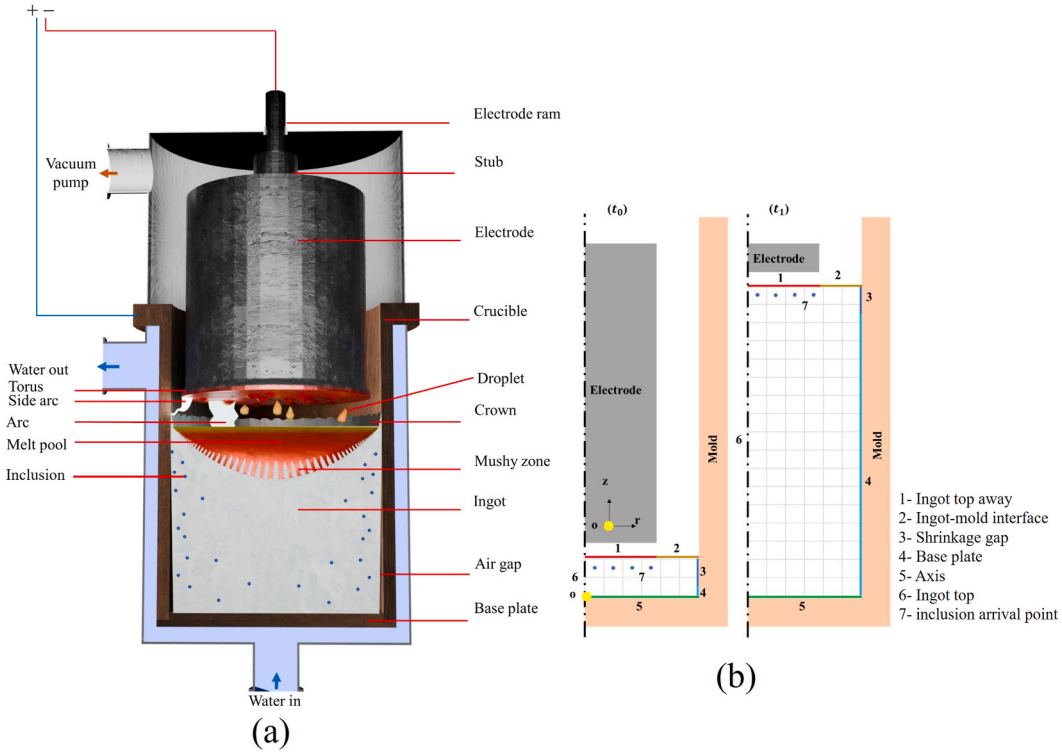

Fig. 1. (a) Schematic representation of the VAR process, illustrating its primary physical phenomena and components. (b) The 2D axisymmetric domain used in the calculation from the base (start stage t_0) to the final height (feeding stage t_1). The grid represents the mesh; for representation purposes, the mesh elements are coarser by a factor of 10 compared to the real simulations.

inclusions are particularly sensitive to current and electrode size, with higher current or smaller electrodes driving them deeper into the ingot. Pan et al. [64] further demonstrated in VAR steel that inclusion density and size critically influence their capture in the mushy-zone.

Despite previous efforts, the effects of side arcing and arc distribution on the evolution and final distribution of inclusions with varying sizes and densities remain insufficiently understood. The present study aims to address this gap by employing transient simulations to examine how inclusions are transported and redistributed throughout ingot growth, from the initial base formation to the final feeding or hot-top stage.

2. Modeling

The numerical model was implemented in a finite-volume computational framework, with user-defined functions developed to account for electromagnetic fields, solidification behavior, inclusion entrapment at the mushy-zone interface, and process-specific arc characteristics such as arc distribution and side arcing. Fig. 1(a) presents a schematic of the VAR setup, illustrating the key phenomena of alloy remelting and solidification. Fig. 1(b) detailed view of the proposed 2D axisymmetric cross-section, highlighting the ingot region and boundaries. The left side shows the mold schematic at t_0 (start of the simulation), while the right side illustrates the model state at t_1 (end of the simulation). The following assumptions were made for the simulations:

I. While the VAR process is inherently three-dimensional, the cylindrical ingot geometry and the primarily azimuthal magnetic field allow it to be reasonably approximated using a 2D axisymmetric model. This approach is widely adopted in VAR studies and enables efficient simulation of transient ingot growth for industrial VAR processes with particle tracking, while maintaining good agreement with experimental observations [40].
II. The calculations are restricted to the ingot domain, with appropriate boundary conditions specified, while the mold, electrode, and plasma are excluded, since the focus of this study is on inclusions within the ingot and melt pool.
III. The electromagnetic field is solved using a one-way coupling approach. This assumption is justified by the low magnetic Reynolds number ($Re_m < 1$), indicating that the influence of fluid motion on the electromagnetic field is negligible under the present VAR conditions [40,65].
IV. Solutal buoyancy is neglected, as melt-pool dynamics are primarily governed by electro-vortex and thermal buoyancy flows, making the influence of composition-driven buoyancy forces negligible [66].
V. The Marangoni effect [67], arising from surface tension and temperature gradients, is neglected, as both the surface tension gradient and the temperature gradient at the melt surface are relatively small. Its influence has been evaluated through additional simulations and confirmed to be negligible, as discussed in Appendix A.
VI. Joule heating is neglected due to the relatively high electrical conductivity of the alloy, which results in low electrical resistance and limited volumetric heat generation compared to the dominant heat input from the arc and droplets [26,68], as discussed in Appendix A.
VII. Molten droplets enter the melt pool beneath the electrode tip and are represented by a uniform mass flow rate [26].
VIII. Inclusions are introduced uniformly into the melt under the shadow of the electrode tip.
IX. The physical properties of the inclusions (size, density, shape, etc.) and their chemical properties (composition, etc.) are assumed to remain unchanged throughout the process.
X. Inclusions are introduced at discrete locations (5 points) and time intervals (100 s) to represent the continuous droplet-driven injection in a time-averaged manner. This approach significantly reduces computational cost while preserving the overall inclusion transport behavior. Additional sensitivity analyses have been performed to evaluate the influence of the number of injection points and injection frequency, confirming that the adopted approach does not affect the overall inclusion distribution, as discussed in Appendix A.
XI. Interdendritic flow was modeled using Darcy's law with Carman–Kozeny permeability [69], and inclusion entrapment is determined based on the liquid fraction (f_l<0.9). Additional sensitivity analyses were performed to evaluate the influence of the entrapment criterion, confirming that the selected threshold does not significantly affect the overall inclusion distribution, as discussed in Appendix A.

2.1. Governing equation

The electromagnetic, thermal–solidification, and flow equations [1]–[16] are listed in Table 1, and the boundary conditions are summarized in Table 2. The detailed descriptions of the governing equations, boundary conditions, and dynamic mesh treatment are identical to those presented in our previous work (Ref. [26]) and are not repeated here. Therefore, only the extensions related to inclusion transport and distribution are discussed in detail here. The transport of inclusions in the VAR melt pool was modeled using the Discrete Phase Model (DPM). The inclusion momentum balance Eq [17]. accounts for drag (Eq [18]), gravity/buoyancy (Eq [19]), pressure gradient (Eq [20]), virtual mass (Eq [21]), and lift forces (Eq [12]) [70]. Turbulent dispersion of inclusions was modeled using the Discrete Random Walk (DRW) model. The instantaneous fluid velocity seen by a particle is expressed as $\boldsymbol{u} = \overline{\boldsymbol{u}} + \boldsymbol{u}'$, where the fluctuating component is given by $\boldsymbol{u}' = \boldsymbol{\zeta}\sqrt{2k/3}$. Here, k is the turbulent kinetic energy obtained from the *SST* k–ω turbulence model [71], and ζ is a vector of random numbers with zero mean and one variance. Particles interact with turbulent eddies over a finite eddy lifetime, after which a new fluctuation is generated, allowing turbulence-induced dispersion to be captured efficiently within the Lagrangian framework. Inclusions are assumed to enter the melt pool 0.5 cm below the ingot top, corresponding to the estimated penetration depth of molten droplets. They are introduced at five discrete locations beneath the electrode tip to represent a time-averaged injection. Injection is performed every 100 s, with a total of 45 inclusions per step. Three particle sizes (1 μm, 12.5 μm, and 25 μm) and three relative densities (0.5, 0.7, and 1.2 times the melt density) are considered based on experimental observations [17].

During the hot topping stage, the heat input at the ingot top is governed by the transient current and melt rate [72], following the same arc-based formulation as in the remelting stage. After the current and melt rate decrease to zero, a radiative heat transfer boundary condition is applied at the top surface to represent cooling (See Table 2).

2.2. Other settings

The material properties of the GH4720Li nickel-based superalloy and the operational conditions, taken from the literature [17,73], are listed in Table 3. Temperature-dependent material properties are implemented using piecewise linear interpolation between the tabulated values.

Herein, the melt rate and current reported in the experiments of Zhao et al. [17] were adopted. Average values during steady ingot growth [74,75] and the actual transient values during hot-topping were used, as shown in Fig. 2(a). An initial small ingot height was chosen as the starting point, and growth was modeled from this height through to the final stage, including hot topping. An initial small ingot height was chosen as the starting point, and growth was modeled from this height through to the final stage, including hot topping. The arc-striking

Table 1
Governing equations of electromagnetic, thermal and solidification, and flow fields.

Electromagnetic field	
$\frac{\partial}{\partial z}\left(\sigma_e\frac{\partial\phi}{\partial z}\right)+\frac{1}{r}\frac{\partial}{\partial r}\left(r\sigma_e\frac{\partial\phi}{\partial z}\right)=0$	[1]
$J_z=-\sigma_e\frac{\partial\phi}{\partial z}$	[2]
$J_r=-\sigma_e\frac{\partial\phi}{\partial r}$	[3]
$B_\theta=\mu_m\frac{1}{r}\int_0^r J_z dr$	[4]
$F_z=J_r\cdot B_\theta$	[5]
$F_r=-J_z\cdot B_\theta$	[6]
Solidification and thermal field	
$\frac{\partial}{\partial t}(\rho h)+\frac{\partial}{\partial z}(\rho u_z h)+\frac{1}{r}\frac{\partial}{\partial r}(\rho r u_r h)=\frac{\partial}{\partial z}\left(\frac{k_{eff}}{C_p}\frac{\partial h}{\partial z}\right)+\frac{1}{r}\frac{\partial}{\partial r}\left(r\frac{k_{eff}}{C_p}\frac{\partial h}{\partial z}\right)+S_h$	[7]
$S_h=-\frac{\partial}{\partial t}(\rho f_l L)-\frac{\partial}{\partial z}(\rho u_z f_l L)-\frac{1}{r}\frac{\partial}{\partial r}(\rho r u_r f_l L)$	[8]
$f_l=\begin{cases}1, T>T_l\\ \left(\frac{T-T_s}{T_l-T_s}\right), T_s<T<T_l\\ 0, T<T_s\end{cases}$	[9]
Flow field	
$\frac{\partial}{\partial t}(\rho)+\frac{\partial}{\partial z}(\rho u_z)+\frac{1}{r}\frac{\partial}{\partial r}(\rho r u_r)=0$	[10]
$\frac{\partial}{\partial t}(\rho u_z)+\frac{\partial}{\partial r}(\rho u_r u_z)+\frac{\partial}{\partial z}(\rho u_z u_z)=-\frac{\partial}{\partial z}(p)+\mu_{eff}\left[\frac{1}{r}\frac{\partial}{\partial r}\left(r\frac{\partial}{\partial r}(u_z)\right)+\frac{\partial^2}{\partial z^2}(u_z)\right]+S_{u_z}$	[11]
$\frac{\partial}{\partial t}(\rho u_r)+\frac{\partial}{\partial r}(\rho u_r u_r)+\frac{\partial}{\partial z}(\rho u_z u_r)=-\frac{\partial}{\partial r}(p)+\mu_{eff}\left[\frac{\partial}{\partial r}\left(\frac{1}{r}\frac{\partial}{\partial r}(ru_r)\right)\right)+\frac{\partial^2}{\partial z^2}(u_r)\Big]+S_{u_r}$	[12]
$S_{u_z}=-\left(\frac{\mu_{eff}}{\kappa}\right)u_z+F_z-g\rho\beta\frac{h-h_{ref}}{C_p}$	[13]
$S_{u_r}=-\left(\frac{\mu_{eff}}{\kappa}\right)u_r+F_r$	[14]
$\frac{\mu_{eff}}{\kappa}=A_{mush}\frac{(1-f_l)^2}{f_l^3}$	[15]
$A_{mush}=1.66\times10^3\frac{\mu_{eff}}{\lambda_1^2}$	[16]

(*continued on next page*)

Table 1 (*continued*)

Electromagnetic field	
Discrete phase model	
$m_p\frac{d\boldsymbol{u_p}}{dt}=\boldsymbol{F_D}+\boldsymbol{F_G}+\boldsymbol{F_B}+\boldsymbol{F_P}+\boldsymbol{F_V}+\boldsymbol{F_L}$	[17]
$\boldsymbol{F_D}=\frac{18\mu}{\rho_p d_p^2}\frac{C_D Re}{24}(\boldsymbol{u}-\boldsymbol{u_p})$	[18]
$\boldsymbol{F_G}+\boldsymbol{F_B}=\frac{g(\rho_p-\rho)}{\rho_p}$	[19]
$\boldsymbol{F_P}=\frac{\rho}{\rho_p}\boldsymbol{u_{p_i}}\frac{\partial\boldsymbol{u}}{\partial x_i}$	[20]
$F_V=\frac{1}{2}\frac{\rho}{\rho_p}\frac{d}{dt}(\boldsymbol{u}-\boldsymbol{u_p})$	[21]
$F_L=\frac{2Kv^{0.5}\rho d_{ij}}{\rho_p d_p(d_{lk}d_{kl})^{0.25}}(\boldsymbol{u}-\boldsymbol{u_p})$	[22]

start-up phase is not included, as a minimum ingot height is required to properly define boundary conditions. While this may influence inclusion entrapment near the ingot bottom, it does not affect the overall inclusion distribution, since the ingot growth rate is very low (~0.05 mm/s). Side arcing [40,41] is implemented by prescribing the electric current distribution through boundary conditions, where a specified fraction of the total current (15%, 40%) is directed through the lateral boundary above the ingot and crown region. This is achieved by adjusting the electric potential at the boundaries, and the corresponding boundary conditions are summarized in Table 2. The arc radius was varied from 25% to 70% of the ingot radius, representing diffusive and constricted arc conditions, respectively. The combined effects of these parameters are illustrated through the Gaussian current distribution at the ingot top, shown in Fig. 2(b).

2.3. Computational procedure

All simulations were performed using the commercial CFD software ANSYS Fluent. Flow, heat transfer/solidification, and electromagnetic fields were discretized using the Finite Volume Method (FVM), while inclusion trajectories were tracked in a Lagrangian framework via the Discrete Phase Model (DPM). Gradient terms were evaluated with the Least Squares Cell-Based method, pressure was discretized using the PRESTO! scheme, and momentum, turbulence (k–ω), energy, and electric potential equations were solved using a Second-Order Upwind scheme. Pressure–velocity coupling was achieved using the SIMPLEC algorithm. All simulations were conducted in transient mode with a time step of 0.1 s. At each time step, 50 iterations were carried out. Convergence was assessed based on residual reduction, with criteria of 10^{-2} for continuity, 10^{-4} for velocity components, 10^{-6} for energy, 10^{-3} for turbulence quantities (k and ω), and 10^{-8} for the electric potential.

A mesh independence study was conducted to ensure numerical accuracy. The results, presented in Appendix A, demonstrate that further mesh refinement does not significantly affect the melt-pool characteristics or inclusion distribution.

Table 2
Boundary conditions of electromagnetic, thermal and solidification, and flow fields, and DPM.

#	Electromagnetic	Thermal and solidification	Flow	DPM
1	$\frac{\partial\varphi}{\partial n} = \frac{I_0\left(1-f_{side-arc}\right)exp\left(-\frac{r^2}{{R_a}^2}\right)}{\int_0^{R_i} 2\pi r exp\left(-\frac{r^2}{{R_a}^2}\right)dr}$	$T = T_L + 400e^{-12\frac{D_i}{J}}$ If $\dot{m}, I = 0$ $Q = \sigma\cdot\varepsilon\left(T^4 - {T_{sur}}^4\right)$	$\boldsymbol{u_z} = \frac{\dot{m}}{\rho\pi {R_e}^2}$	*reflect*
2	$\frac{\partial\varphi}{\partial n} = \frac{I_0\left(1-f_{side-arc}\right)exp\left(-\frac{r^2}{{R_a}^2}\right)}{\int_0^{R_i} 2\pi r exp\left(-\frac{r^2}{{R_a}^2}\right)dr}$	$T = T_L + 400e^{-12\frac{D_i}{J}\left(\frac{R_m-2r}{R_m-R_e}\right)}$ If $\dot{m}, I = 0$ $Q = \sigma\cdot\varepsilon\left(T^4 - {T_{sur}}^4\right)$	$\frac{\partial \boldsymbol{u_r}}{\partial r} = \boldsymbol{u_z} = 0$	*reflect*
3	$\varphi = 0$	$HTC = 500\ Wm^{-2}K^{-1}$	$\boldsymbol{u_{r,z}} = 0$	*reflect*
4	$\frac{\partial\varphi}{\partial n} = 0$	$Q = \sigma\cdot\varepsilon\left(T^4 - {T_{sur}}^4\right)$	$\boldsymbol{u_{r,z}} = 0$	*reflect*
5	$\varphi = 0$	$HTC = 500\ Wm^{-2}K^{-1}$	$\boldsymbol{u_{r,z}} = 0$	*reflect*
6	*Axis*	*Axis*	*Axis*	*Axis*

Table 3
Parameters used in the simulation.

Material properties, Symbol, Unit	Value
Electric conductivity, σ_e, $\Omega^{-1}\cdot m^{-1}$	9.5×10^5
The magnetic permeability, μ_m, $J.m^{-1}\cdot A^{-2}$	$4\pi\times10^{-7}$
Liquid Density, ρ, $kg\cdot m^{-3}$	8100.0
Solid Density, ρ, $kg\cdot m^{-3}$	7210.0
Effective thermal conductivity, k_{eff}, $W.kg^{-1}\cdot m^{-1}$	(673.0 K,17.10),(1073.0 K,23.85), (1473.0 K,30.45),(1553.0 K,30.97), (1673.0 K,29.66),(1773.0 K,31.30)
Heat capacity, C_p, $J.kg^{-1}\cdot K^{-1}$	(673.0 K,523.80),(1073.0 K,650.80), (1473.0 K,731.50),(1553.0 K,743.90), (1673.0 K,780.50),(1773.0 K,803.80)
Surface tension gradient, $\frac{d\gamma}{dT}$, $N.m^{-1}\cdot K^{-1}$	(1532.0 K,0.00019),(1603.0 K,0.00019), (1902.0 K,-0.00019),(2500.0 K,-0.00019),
Latent heat of solidification, L, $J\cdot kg^{-1}$	245000.0
Liquidus temperature, T_l, K	1611.0
Solidus temperature, T_s, K	1467.0
Thermal expansion, β, K^{-1}	1.36×10^{-4}
Primary dendrite arm spacing (min,Max), λ_1, m	$(250.0,640.0)\times10^{-6}$
Effective viscosity, μ_{eff}, $Pa\cdot s$	5.3×10^{-3}
Gravitational acceleration, g, $m\cdot s^{-2}$	9.81
Operation condition, Symbol, Unit	Value
Total imposed current, I_0, A	variable,See Fig.2(a)
Voltage, v,V	23.2
Radius of ingot, R_i, m	0.254
Ingot height, h_{ingot} (min,Max), m	0.04,1.35
Radius of mold, R_m, m	0.279
Radius of electrode, R_e, m	0.220
Mass flow rate, $\dot{m}$, $kg\cdot min^{-1}$	variable,See Fig. 2(a)

3. Results

3.1. Transient ingot growth

Here, the capability of the proposed model to capture transport phenomena, including fluid flow, thermal and solidification behavior, electromagnetic fields, and inclusion distribution are demonstrated. Fig. 3(a) presents simulation results for a side-arcing intensity of 15% and an arc ratio of 70% (diffusive arc), showing (from left to right) the distributions of current density, magnetic field, Lorentz force, and velocity, along with white iso-lines of the liquid fraction at 0.97 and 0.06.

The current intensity is highest at the top of the ingot due to the Gaussian arc distribution and the additional current entering through the ingot–mold interface, which together generate stronger magnetic fields. The interaction between the magnetic field and the electric current produces a Lorentz force that is also most pronounced near the top, directed from the ingot's outer surface toward its axis. Herein, the thermally driven buoyancy flow is significantly stronger than the electro-vortex flow, as demonstrated in Appendix A. Therefore, only a single dominant vortex is observed in the domain, as indicated by the yellow streamlines in the velocity contour. Because the structures of the current, magnetic field, Lorentz force, and velocity remain almost constant during ingot growth, a single representative snapshot is presented for clarity.

The evolution of the melt pool depth, defined by the liquidus (f_l=0.97) and solidus (f_l=0.06) lines throughout the process, is shown in Fig. 3(b), where the pool depth increases progressively until the ingot height reaches approximately 0.6 m, about 1.2 times the ingot diameter, after which a steady state is established. This steady condition persists until the onset of the hot-topping stage, during which the pool depth begins to decrease. As shown in Fig. 3(c), snapshots at different times and heights are presented. These snapshots display the temperature field on the left and the liquid fraction on the right. At the early stage, when the ingot is short, base plate cooling dominates, producing a shallower pool; as the ingot grows, the influence of base cooling decreases, and the melt pool correspondingly deepens [76].

Fig. 4(a) illustrates the distribution of inclusions within the VAR melt pool during ingot growth up to a height of 1 m, at which a steady melt pool has already been established. The four panels, from left to right, show the spatial distribution of inclusion diameter, density, residence time, and inclusion mass. In all cases, a pronounced accumulation of inclusions is observed along the ingot wall. These inclusions become trapped within the mushy-zone and ultimately remain in the solidified ingot.

The peripheral entrapment is primarily governed by the melt flow field established under the selected operating conditions i.e. side-arcing intensity of 15% and an arc ratio of 70% (diffusive arc). Thermal buoyancy generates a dominant outward flow that transports the majority of inclusions toward the wall shortly after entering the pool. Only a smaller fraction of inclusions is able to penetrate deeper into the molten region. In the lower part of the melt pool, where flow velocities are relatively low, inclusion motion becomes more sensitive to particle mass. Lighter inclusions can be transported upward by the local flow, whereas heavier inclusions tend to remain in deeper regions and accumulate closer to the ingot center before eventually being captured by the mushy-zone.

To quantify the distribution patterns, the ingot radius was discretized into ten concentric segments with uniform radial spacing (Δr). Fig. 4(b) presents the percentage of total inclusion accumulation up to a height of 1 m, along with the corresponding radial fraction of captured inclusions for all inclusion sizes and densities considered. Independent of inclusion properties, the radial profiles consistently exhibit strong peripheral enrichment. In the inner region of the ingot, only negligible inclusion entrapment is observed, while a gradual increase appears toward intermediate areas. A pronounced accumulation occurs close to the ingot

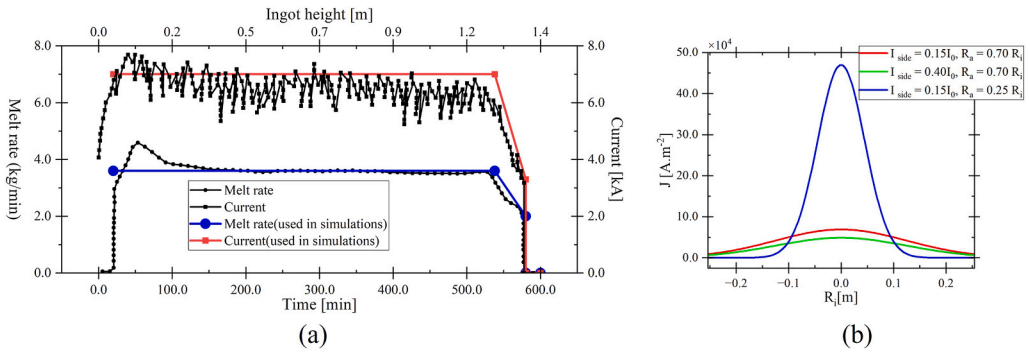

Fig. 2. (a) Melt rate and current from the experiments and the corresponding values used in the simulations. (b) *Arc distribution* above the ingot top, represented by Gaussian profiles for three different scenarios.

wall, where inclusions preferentially concentrate, increasing from below ~1% in the inner region to approximately 13–15% near the ingot edge, as illustrated in Fig. 4(b).

A detailed analysis of the forces acting on inclusions and their transport trajectories is provided in Appendix A (Figure A9). The results show that inclusion motion is primarily governed by drag force, driven by the outward thermal buoyancy flow, which dominates the melt-pool dynamics under the present conditions. Gravity and buoyancy forces contribute as secondary effects, while pressure gradient, virtual mass, and Saffman lift forces are comparatively small. As a result, inclusions are transported outward toward the ingot sidewall and follow recirculating paths within the melt-pool vortex before being captured in the mushy zone. This confirms that inclusion transport is predominantly controlled by the flow field through drag-dominated dynamics.

Overall, the quantitative results reinforce that thermal-buoyancy-driven melt flow due to diffusive arc governs inclusion migration, leading to weak central entrapment and strong wall-side accumulation across all inclusion sizes and densities.

To effectively visualize the transient ingot growth, videos of the above case are provided as supplementary material. These recordings present the dynamic evolution of both the fields and inclusions.

3.2. Experimental validation

Two key parameters were selected to validate the simulation results against the experimental measurements of Zhao et al. [17]: the

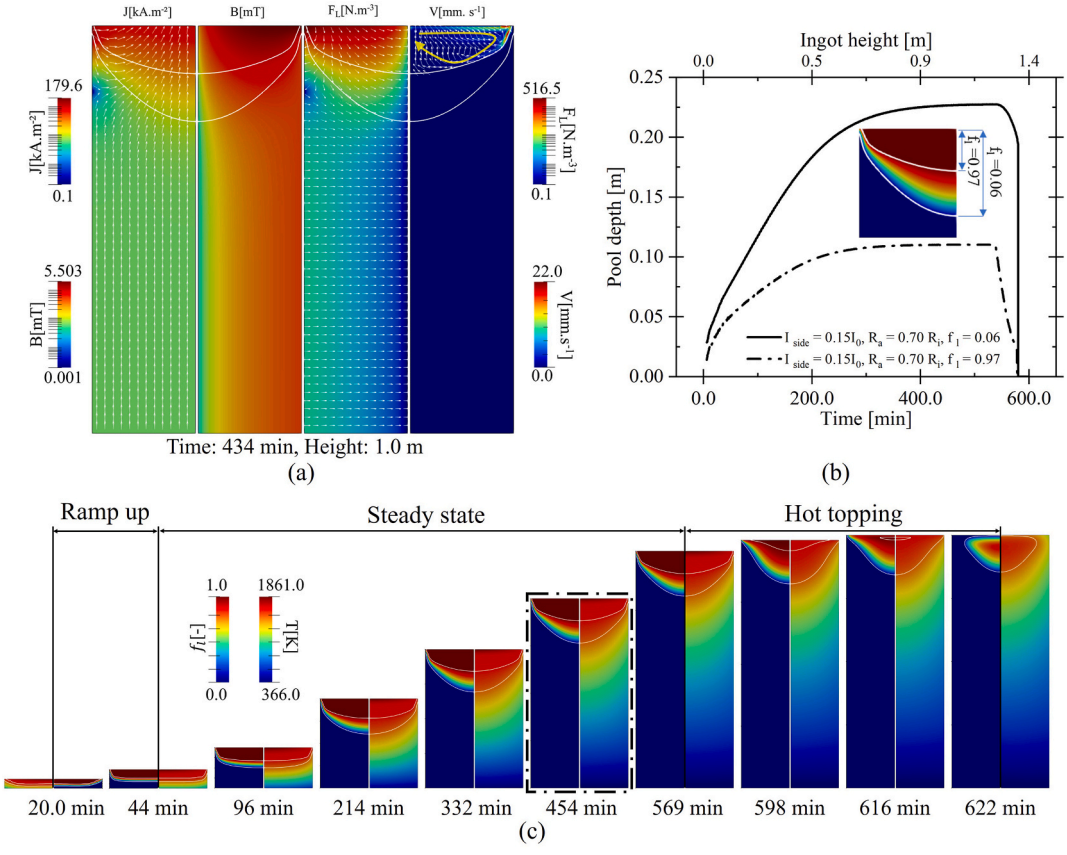

Fig. 3. (a) Field distributions of current density, magnetic field, Lorentz force, and velocity (from left to right) for 15% side arcing and a 70% arc ratio, with iso-lines of liquid fraction 0.97 and 0.06. (b) Evolution of liquidus and solidus pool depths throughout the process, showing pool growth, steady state, and the decrease during hot topping. (c) Snapshots at different times and ingot heights showing temperature (left) and liquid fraction (right) fields, with the mushy-zone indicated by two white iso-lines.

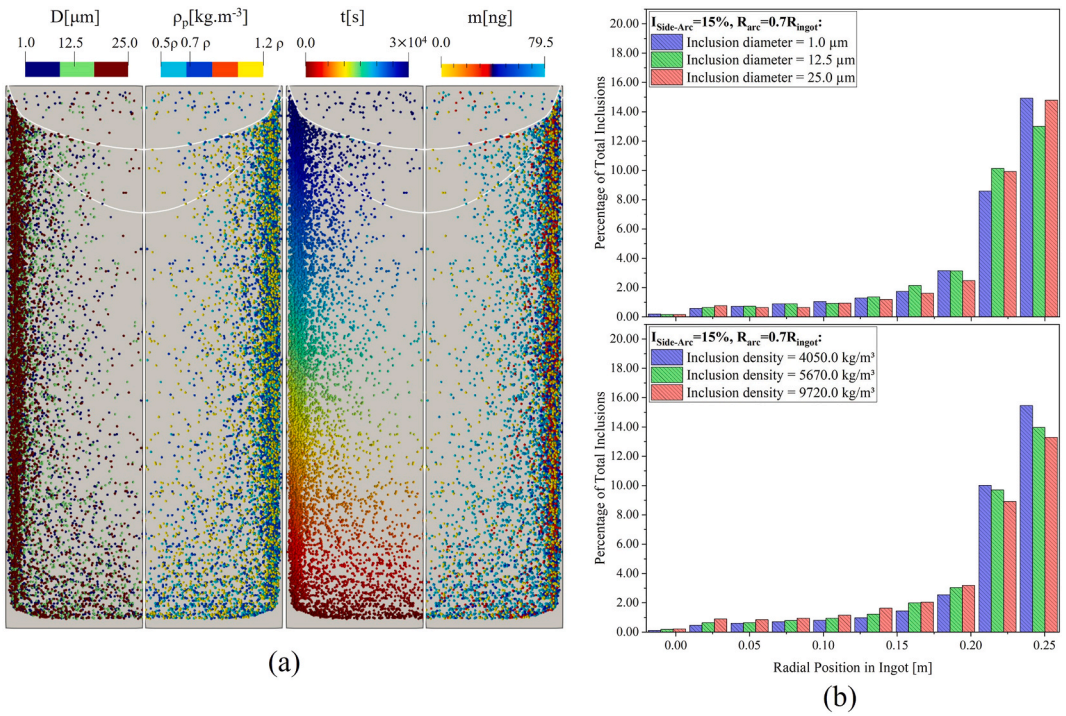

Fig. 4. (a) Distributions of inclusions within the ingot based on inclusion diameter, density, residence time, and mass (from left to right) for a 15% side-arcing condition and a 70% arc ratio, with iso-lines of liquid fraction 0.97 and 0.06 indicating the liquidus and solidus boundaries. (b) Quantitative radial distribution of captured inclusions for the different inclusion sizes and densities.

melt-pool depth and the radial number density of inclusions at different solidification stages.

Fig. 5(a) shows the temporal evolution of the melt-pool depth along the ingot height for a side-arcing intensity of 15% and an arc ratio of 70%. Both the liquidus contour (liquid fraction f_l=0.97) and the solidus contour (liquid fraction f_l=0.06) are reported and compared with the experimental measurements of Zhao et al. [17] The simulated liquidus profile slightly overpredicts the pool depth, whereas the solidus profile shows good agreement with the experimental data throughout most of the ingot height. This indicates that the model captures the overall pool shape and solidification front evolution with reasonable accuracy under the selected operating conditions.

Fig. 5(c) compares the simulated and experimental number density of inclusions at three radial locations. In the experiment, cubic samples of 10×10×10 mm were extracted at an ingot height of approximately 0.65 m, corresponding to three radial positions: center, mid-radius, and near the ingot edge (As shown in Fig. 5(b)). Since the exact radial location of the edge sample was not explicitly reported, it was assumed to be located slightly inward from the ingot sidewall (2 cm). This assumption is physically reasonable because the true ingot edge contains the crown region, where high porosity makes accurate inclusion density measurements extremely difficult. In practice, experimental samples are obtained after machining the crown, resulting in an effective sampling radius slightly inside the nominal ingot radius.

The experimental data show that the number density of small inclusions increases from the center toward the ingot periphery. A similar trend is observed for medium-sized inclusions. In contrast, the number density of large inclusions decreases toward the ingot edge. The simulation reproduces the increasing trend from the center to the mid-radius for all inclusion sizes, followed by a strong increase toward the ingot side. Good agreement is obtained for small and medium inclusions at the center and mid-radius positions, as shown in Fig. 5(b). For large inclusions, the simulation matches the experimental values well at the center and mid-radius but predicts an increase toward the edge, whereas the experiment shows a decrease. Consequently, the discrepancy between simulation and experiment becomes more pronounced near the ingot side wall.

The discrepancy observed for larger inclusions near the ingot edge is attributed to limitations of the current modeling framework as well as the nature of the available experimental data. Although additional analyses were performed (Appendix A), including the effects of Joule heating, Marangoni forces, entrapment criteria, mesh resolution, and injection strategy, the overall trend of peripheral accumulation remained unchanged. This suggests that the deviation is likely related to physical mechanisms not captured in the model. In particular, the mushy-zone characteristics near the ingot top, where strong cooling leads to finer dendritic structures and steep temperature gradients, may reduce the probability of capturing larger inclusions, allowing them to penetrate deeper into the melt pool before entrapment. Furthermore, the absence of dendrite-scale modeling and microsegregation limits the accurate representation of particle–interface interactions. Potential effects associated with crown and shelf regions, which are not included in the present model, may further influence inclusion capture behavior. In addition, the experimental data are based on measurements at specific sampling locations, which may not fully represent the global inclusion distribution within the ingot.

The present model accounts for two major sources of uncertainty widely discussed in VAR literature: the arc distribution above the ingot surface 26,44,77–79 and the magnitude of side arcing [26,40–42, 80–82]. These uncertainties stem from the complex behavior of the vacuum arc, which can shift between centric, eccentric, diffuse, or constricted modes, and from process variations such as changes in crown height [42], the formation and evolution of the shrinkage gap [43], and the continuously increasing ingot height. The following sections address parametric studies on side arcing, arc distribution, and inclusion entry location associated with drip-short events.

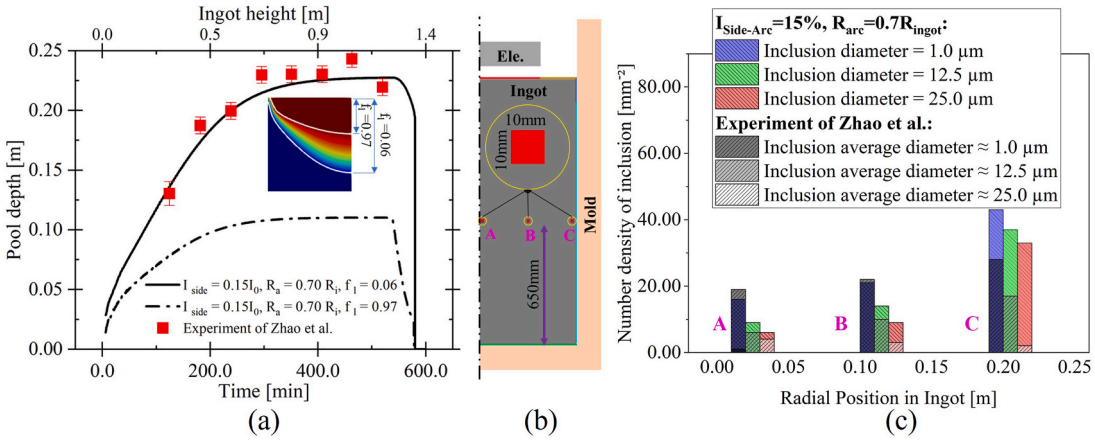

Fig. 5. (a) validation of the numerical model against the experimental data of Zhao et al. [33]: evolution of melt-pool depth along the ingot height for side-arcing intensity of 15% and an arc ratio of 70% side-arcing, showing the liquidus (f_l=0.97) and solidus (f_l=0.06) contours; (b) Locations and total counts of sampling stations for experimental validation and simulation data extraction; (b) comparison of simulated and experimental radial number density of inclusions for different inclusion sizes at an ingot height of approximately 0.65 m.

4. Discussions

4.1. Effects of side arcing

Fig. 6(a)–(c) illustrate the effect of side-arcing intensity on melt-pool flow, inclusion transport, and radial inclusion distribution for an arc ratio of 70% (diffusive arc). Fig. 6(a) presents a side-by-side comparison of the melt-pool velocity fields for side-arcing intensities of side-arcing intensity of 15% (left) and side-arcing intensity of 40% (right). At the lower side-arcing level, the flow is dominated by thermal buoyancy, producing a broad outward circulation and a deeper melt pool. Increasing the side-arcing intensity reduces the heat intensity above the ingot top, weakens the buoyancy-driven flow, and leads to a slightly shallower and narrower liquid pool. Despite these quantitative changes, the overall flow topology remains similar, with the primary effect being a redistribution of flow strength near the melt surface.

The corresponding spatial distributions of inclusions are shown in Fig. 6(b) for both side-arcing intensities. When the side-arcing intensity is increased, the reduced heat input near the ingot top causes the liquid pool profile to shift inward, toward the ingot center. As a consequence, inclusions encounter the trapping condition defined by the liquidus profile earlier along their trajectories and are captured before reaching the sidewall. This leads to a redistribution of inclusions, with the region of maximum accumulation forming at a finite distance from the ingot wall rather than directly at the outer radius. This behavior is consistently observed for both diameter-dependent and density-dependent inclusion distributions. Fig. 6(c) quantifies these trends by comparing the radial fraction of captured inclusions for the two side-arcing intensities. For side-arcing intensity of 15%, the inclusion fraction increases monotonically toward the ingot edge, reaching its maximum at the outer radius (~14–15%). In contrast, for side-arcing intensity of 40%, the peak inclusion concentration shifts inward (r≈0.20–0.22 m), and the inclusion fraction at the ingot wall is reduced to approximately ~2–3%. This inward shift of the accumulation zone occurs for all inclusion sizes and densities, while the central region of the ingot exhibits a significantly lower inclusion number density.

4.2. Effects of arc distribution

Fig. 7(a) compares the melt-pool velocity fields for two arc-distribution scenarios while keeping the side-arcing intensity constant at 15% of the total current. The left panel corresponds to the baseline case with a diffusive arc distribution and an arc ratio of 70% (diffusive arc), whereas the right panel shows the constricted-arc configuration with an arc ratio of 25% (constricted arc). When the arc distribution is constricted, the electrovortex flow becomes significantly stronger, as highlighted by the red isoline. The intensified electrovortex expands toward the pool axis and displaces the thermally driven circulation toward the sidewalls. Consequently, the flow in the constricted-arc case becomes more confined to the central region of the pool, with higher peak velocities and a more pronounced inward jet beneath the arc. These changes in the melt-pool flow structure are expected to strongly influence inclusion transport and entrapment. Fig. 7(b) compares the inclusion distributions for diffusive and constricted arc configurations. Concentration of arc energy toward the pool center enhances central heating and reduces thermal input near the sidewalls, resulting in a narrower melt pool and an inward shift of the liquidus contour. As a result, inclusions encounter the trapping condition earlier along their trajectories and are captured before reaching the ingot wall. Consequently, the region of maximum inclusion accumulation shifts inward relative to the baseline case, and the inclusion number density near the ingot wall is reduced. Inclusion concentrations become more localized in the lower side region of the ingot, with fewer inclusions penetrating into the mid-radius region of the melt pool.

The inward accumulation of inclusions observed in the lower part of the ingot under constricted arc conditions (arc ratio = 25%) (Fig. 7(b)) can be attributed to the combined effects of thermal buoyancy flow, electro-vortex flow, and the evolution of the solidification front. At early stages, the melt pool exhibits a U-shaped profile, and the mushy zone near the top of the ingot is relatively thick, promoting early capture of inclusions. As the ingot height increases, the mushy zone near the top becomes thinner, allowing inclusions to penetrate deeper into the melt pool before being captured. Fig. 7(c) compares the radial distribution of captured inclusions for the diffusive (arc ratio of 70%) and constricted arc (arc ratio of 25%) configurations. In the diffusive-arc case, inclusions preferentially accumulate near the ingot wall, reaching approximately ~14–15% at r≈0.25 m. Under arc constriction, however, the reduced outward flow limits radial transport, causing inclusions to be captured earlier within the melt pool, with peak accumulation shifting inward to r≈0.18–0.22 m and the wall fraction reduced to ~ 9–12%. Consequently, the region of inclusion accumulation shifts away from the ingot sidewall toward the interior, and the fraction of inclusions entrapped in the inner melt-pool region increases relative to the diffusive-arc case.

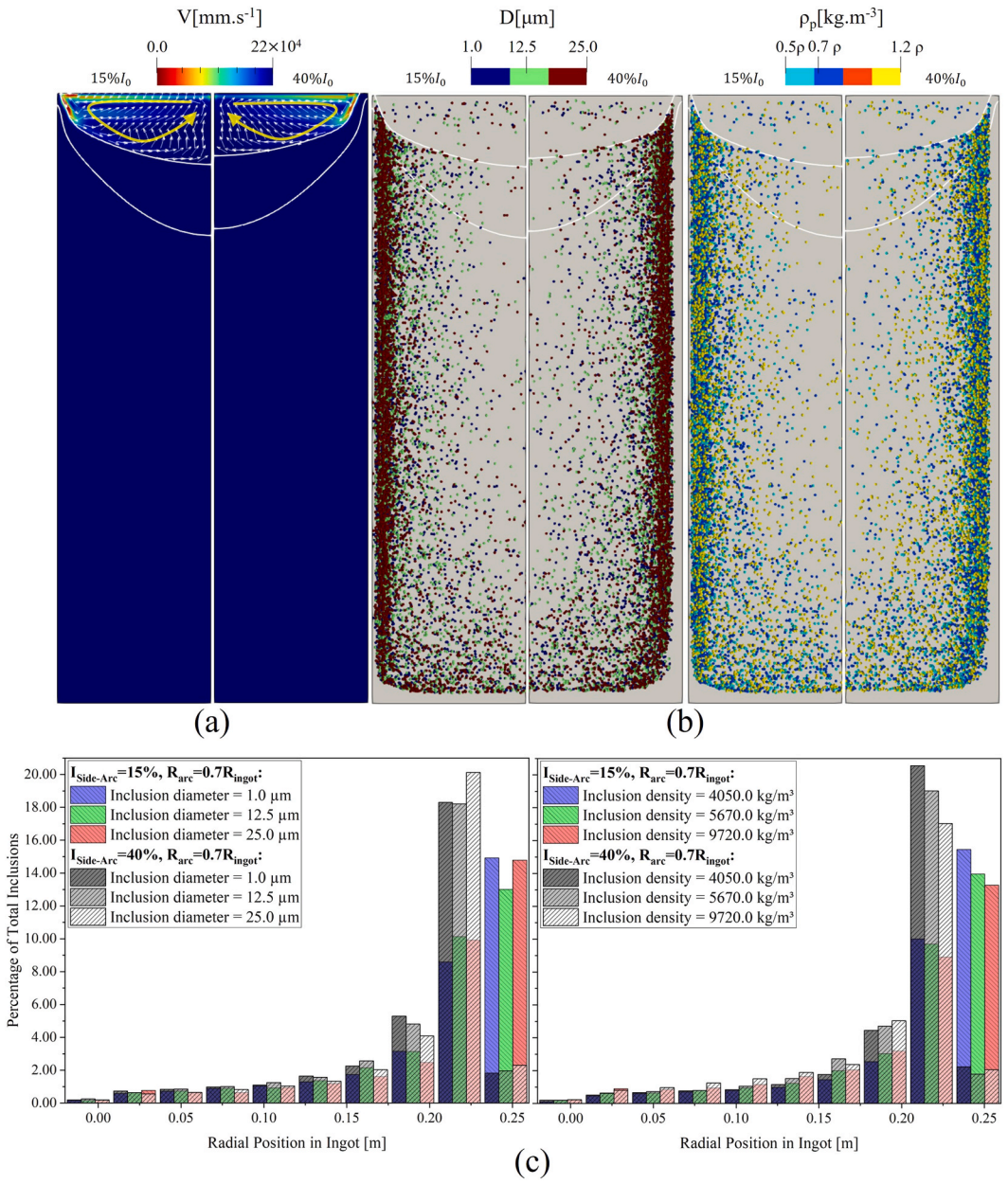

Fig. 6. (a) Comparison of melt-pool velocity fields for the side arcing of 15% (left) and 40% (right) configurations, white isolines indicate the liquidus and mushy-zone boundaries; (b) side-by-side spatial distributions of inclusions colored by inclusion diameter and inclusion density; (c) corresponding radial distributions of captured inclusions.

4.3. Effect of inclusion entry location

During normal VAR operation, exogenous inclusions typically enter the melt pool from the electrode tip region. During a drip-short event [83], a large amount of current can pass through a very narrow liquid column, leading to locally increased current density, enhanced Lorentz forces, and significantly higher melt velocities. These transient effects can promote deeper inclusion penetration and altered trajectories. In the present study, these complex transient phenomena are not explicitly resolved; instead, their effect is approximated by introducing inclusions at a deeper location. To investigate this influence, an additional simulation was performed in which inclusions were introduced from a position 5 cm below the ingot top, instead of the standard 0.5 cm below the ingot top.

Fig. 8(a) shows the resulting spatial distribution of inclusions for the drip-short-like entry location, displayed for inclusion diameter, density, residence time, and inclusion mass. In the baseline configuration, the velocity contours reveal a strong outward vortex near the melt surface; its maximum strength occurs close to the ingot top and rapidly drives newly injected inclusions toward the sidewall, producing a pronounced concentration of inclusions in that region. When inclusions are injected 5 cm deeper, the influence of this surface vortex is substantially reduced. As a result, more inclusions are able to descend into the melt before being redirected toward ingot surface, and the overall inclusion distribution becomes noticeably more diffuse than in the baseline case. Despite this enhanced penetration, inclusions are still ultimately transported outward and captured within the mushy-zone near the ingot wall, although the capture region is more vertically distributed than in the

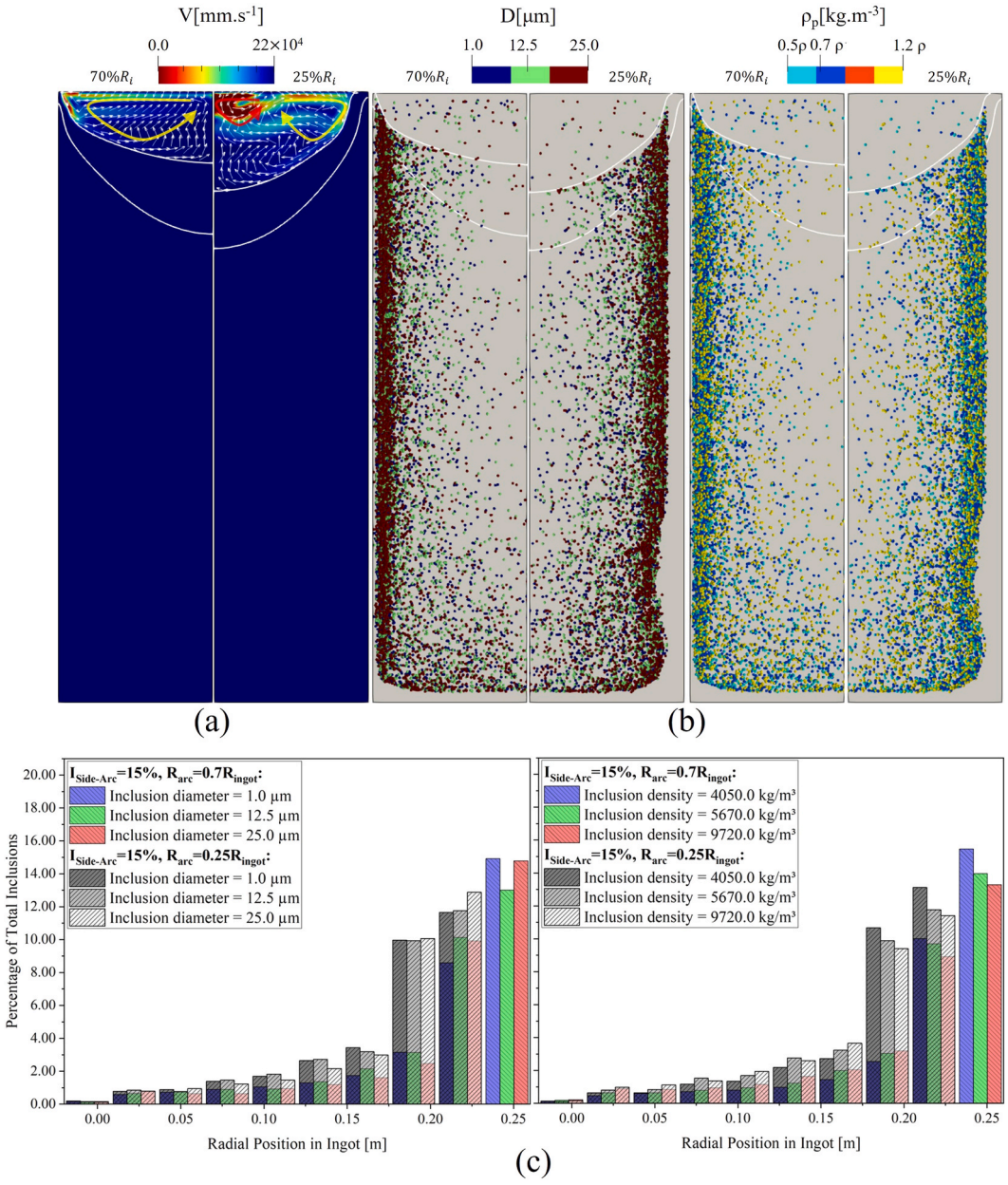

Fig. 7. (a) Comparison of melt-pool velocity fields for the diffusive-arc ($R_a = 0.7R_i$) and constricted-arc ($R_a = 0.25R_i$) configurations, White isolines indicate the liquidus and mushy-zone boundaries; (b) side-by-side spatial distributions of inclusions colored by inclusion diameter and inclusion density; (c) corresponding radial distributions of captured inclusions.

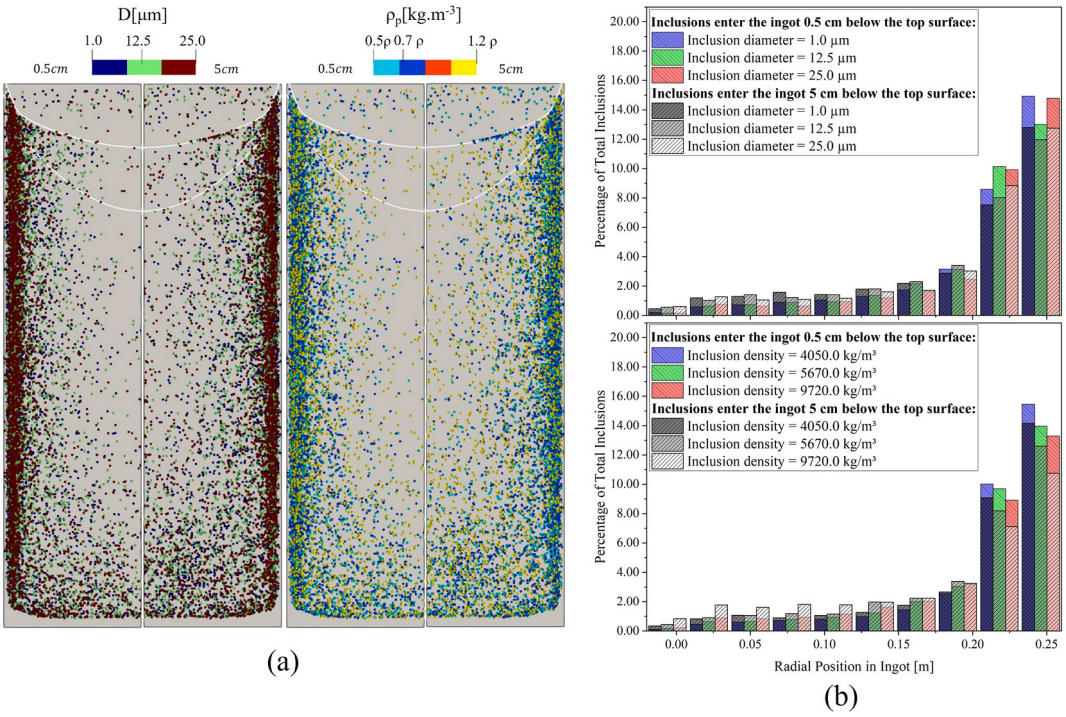

Fig. 8. (a) spatial distribution of inclusions for the deeper (5 cm) entry location case, shown for inclusion diameter, inclusion density, residence time, and inclusion mass; (b) corresponding radial inclusion fractions for both entry location (5 cm and 0.5 cm). White isolines indicate the mushy-zone.

standard entry location case. Fig. 8(b) compares the radial distribution of captured inclusions for inclusion arrival depths of 0.5 cm and 5 cm, shown separately for inclusion size and density. In both cases, inclusion content increases toward the ingot wall; however, deeper inclusion entry reduces near-wall accumulation from approximately ~14–15% to ~12–13% at r≈0.25 m and leads to a more diffuse radial distribution. At the same time, inclusion fractions in the intermediate region (r≈0.15–0.20 m) increase by about ~ 1–2%, indicating enhanced penetration into the melt prior to interception by the mushy-zone.

From an industrial perspective, inclusion accumulation near the ingot periphery is advantageous, as surface inclusions can be removed during subsequent machining operations. In contrast, inclusions entrapped within the ingot interior remain in the final product and directly compromise material cleanliness and mechanical performance. Based on the present results, lower side-arcing intensity combined with a diffusive arc distribution is preferable, as it promotes peripheral inclusion accumulation. In contrast, higher side-arcing intensity or arc constriction shifts inclusion entrapment toward the ingot interior. In industrial practice, arc distribution can be influenced by process parameters such as arc gap and the application of axial magnetic fields. More recently, horizontal magnetic fields have also been deliberately introduced to stabilize arc behavior during the VAR process.

Future studies should incorporate endogenous inclusion formation through coupling with solute transport and segregation 84–86, as well as inclusion dissolution in the melt pool, and the influence of crown and shelf regions on entrapment behavior. Such investigations would provide a more comprehensive understanding of inclusion transport and refining efficiency in VAR under industrial operating conditions.

5. Conclusions

A numerical framework was developed to investigate the transport and entrapment of exogenous inclusions during VAR over the full ingot growth process. The novelty of this work lies in the transient simulation of inclusion behavior throughout the entire ingot growth, combined with a systematic investigation of arc distribution and side-arcing effects. The model was validated against experimental measurements of melt-pool depth and radial inclusion number density, showing good agreement with reported trends. Based on the validated simulations, a series of parametric studies was performed to quantify the influence of key operational parameters on inclusion distribution. The main findings of this work can be summarized as follows:

- Higher side-arcing intensity weakens the electro-vortex flow (EVF), making thermal buoyancy dominant, resulting in a shallower melt pool and shifting inclusion accumulation inward while reducing wall concentration.
- A constricted arc strengthens the electro-vortex flow (EVF), leading to a deeper melt pool, weakening peripheral accumulation, and promoting a more distributed inclusion profile toward the center.
- Deeper inclusion arrival location, representative of drip-short conditions, increases inclusion penetration depth and broadens the spatial and radial distribution of inclusions.

Overall, the results demonstrate that inclusion distribution in VAR is strongly governed by melt-pool geometry, flow structure, and inclusion entry conditions. Operational parameters such as side arcing and arc distribution, which determine the spatial current density profile and can be controlled, for instance, by applying an axial magnetic field, directly affect inclusion transport trajectories and the location of final entrapment. From a practical perspective, a diffusive arc combined with lower side-arcing intensity is preferable, as it promotes peripheral inclusion accumulation that can be removed during machining. In contrast, higher side-arcing intensity or arc constriction shifts inclusions toward the ingot interior, which is less desirable for material cleanliness.

Nomenclature

A_{mush}	Mushy-zone coefficient, $kg{\cdot}m^{-3}{\cdot}s^{-1}$
B_θ	Magnetic flux density in the tangential direction, T
C_p	Heat capacity, $J.kg^{-1}{\cdot}K^{-1}$
d_{ij}	deformation tensor, s^{-1}
$d_{kl}d_{lk}$	strain-rate tensor, s^{-2}
f_l	The volume fraction of liquid, –
f_R	Arc ratio, –
$f_{side-arc}$	Fraction of electric current as side arcing, –
F_z, F_r	Lorentz force in the axial and the radial direction, $N{\cdot}m^3$
F_D	Drag force, N
F_G	Gravity force, N
F_B	Buoyancy force, N
F_P	Pressure force, N
F_V	virtual mass force, N
F_L	Saffman's lift force, N
g	Gravitational acceleration, $m{\cdot}s^{-2}$
h	Local enthalpy, $J{\cdot}kg^{-1}$
h_{ideal}	The height of the defined mesh size, m
h_{ingot}	Ingot height, m
h_{mesh}	The height of the new layer of mesh, m
h_{ref}	Reference enthalpy, $J{\cdot}kg^{-1}$
i, j	Unit vectors in axial, and radial directions, –
I_0	Total imposed current, A
J_z, J_r	Electric current density in the axial and the radial direction, $A{\cdot}m^{-2}$
k_{eff}	Effective thermal conductivity, $W.kg^{-1}{\cdot}m^{-1}$
k	Turbulent kinetic energy
I	Electric current intensity, kA
L	Latent heat of solidification, $J{\cdot}kg^{-1}$
$\dot{m}$	Mass flow rate, $kg{\cdot}min^{-1}$
m_p	Mass of particle
p	Pressure, $N{\cdot}m^{-2}$
R_a	Radius of arc, m
R_e	Radius of electrode, m
R_i	Radius of ingot, m
R_m	Radius of mold, m
S_h	Enthalpy source term, $J{\cdot}m^{-3}.s^{-1}$
S_{u_z}, S_{u_r}	Axial and radial velocity source term, $N{\cdot}m^{-3}$
T	Temperature, K
T_l	Liquidus temperature, K
T_s	Solidus temperature, K
T_{sur}	Surrounding temperature, K
u_{mesh}	Velocity of dynamic mesh, $m{\cdot}s^{-1}$
u_z, u_r	Axial and radial velocity, $m{\cdot}s^{-1}$
u_p	Velocity of particle
v	Voltage, V
z, r	Coordinate in the axial and the radial direction of the ingot, m
α_c	Split factor, m
β	Thermal expansion, K^{-1}
ε	Emissivity, –
γ	Surface tension, γ, $N.m^{-1}$
ζ	Vector of random numbers between 0 and 1, –
κ	Permeability, m^2
λ_1	Primary dendrite arm spacing, m
σ	Stefan-Boltzmann constant, $Wm^{-2}{\cdot}K^{-4}$
σ_e	Electric conductivity, $\Omega^{-1}{\cdot}m^{-1}$
μ_{eff}	Effective viscosity, $Pa{\cdot}s$
μ_m	The magnetic permeability, $J.m^{-1}{\cdot}A^{-2}$
ρ	Density, $kg{\cdot}m^{-3}$
ρ_p	Density of particle, $kg{\cdot}m^{-3}$
τ_{Mar}	Marangoni stress, $N{\cdot}m^{-2}$
ϕ	Electrical potential, V
ω	Specific rate of dissipation

Declaration of competing interest

The authors declare that they have no known competing financial interests or personal relationships that could have appeared to influence the work reported in this paper.

Appendix A. Supplementary data

Supplementary data to this article can be found online at https://doi.org/10.1016/j.jmrt.2026.04.262.

Appendix A

To assess the robustness of the adopted modeling assumptions and numerical settings, a series of additional simulations were performed. The investigated parameters include mesh resolution, the influence of additional physical effects, and key modeling inputs related to inclusion injection and entrapment. Specifically, the following aspects were examined: mesh independence through comparison with a 30% coarser and a 30% finer mesh; the influence of Marangoni forces; the effect of Joule heating; the number of inclusion injection points (increased from 5 to 20); the injection frequency (reduced from 100 s to 50 s); and the criterion for inclusion entrapment in the mushy zone (liquid fraction threshold increased from 0.9 to 0.95). The results of these analyses are presented and discussed in the following subsections.

A. Mesh Independence Study

A mesh independence study was conducted to evaluate the influence of spatial discretization on the numerical results. In addition to the baseline mesh (element size 5 mm ×5mm), two additional meshes were generated: one with 30% fewer elements (coarser mesh) and one with 30% more elements (finer mesh). All simulations were performed under identical boundary conditions and numerical settings to ensure a consistent comparison. The key flow and inclusion transport characteristics were analyzed to assess the sensitivity of the model to mesh resolution.

Figure A1 presents a comparison between the baseline mesh (5 mm) and a case with a 30% coarser mesh. Figure A1(a) shows a zoomed view of the liquid fraction contour together with the mesh elements in the mushy zone for both cases. As the mesh becomes coarser, a slight increase in melt-pool depth is observed; however, this variation remains within the order of the local cell size. Figure A1(b) illustrates the velocity field in the melt pool, indicating that the overall flow structure remains consistent between the two cases. Figure A1(c) shows the inclusion distribution for different particle sizes and densities, where the general distribution pattern remains similar. For a more quantitative comparison, Figure A1(d) presents the statistical distribution of inclusions. With increasing mesh size, inclusions tend to be captured slightly earlier, resulting in a small reduction in inclusion fraction near the ingot wall. This discrepancy gradually diminishes toward the inner regions of the ingot.

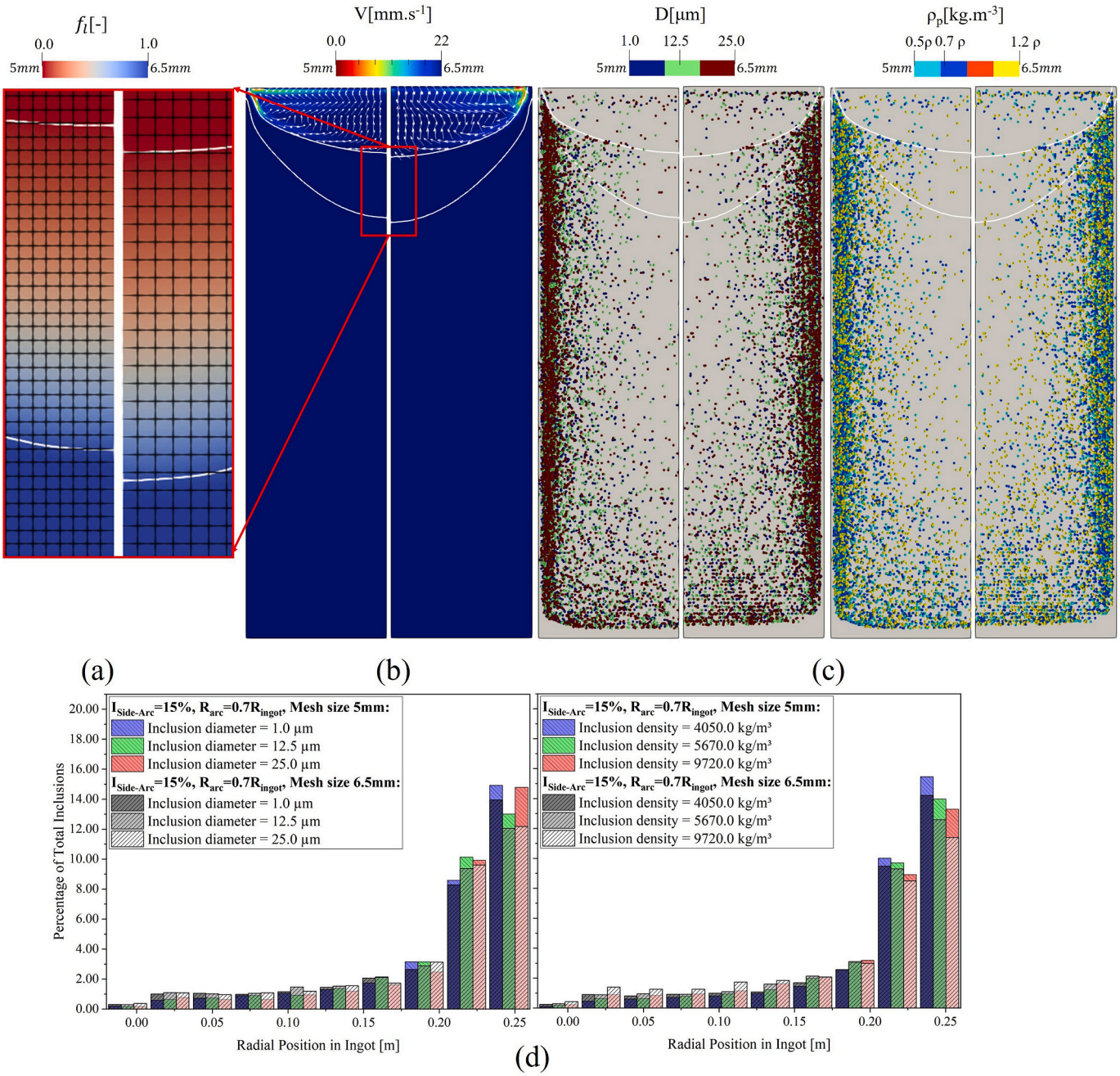

Fig. A1. Comparison of mesh sensitivity between the baseline mesh (5 mm) and a 30% coarser mesh: (a) Liquid fraction contour with mesh distribution, zoomed-in view of the mushy zone, (b) velocity field in the melt pool, (c) inclusion distribution for different particle sizes and densities, and (d) statistical radial distribution of inclusions.

Figure A2 presents the comparison between the baseline mesh and a 30% finer mesh. Similar contour plots and overall trends are observed across all evaluated fields. A slight reduction in melt-pool depth is noted with the finer mesh; however, this variation remains within the order of the mesh size. The inclusion distribution, as shown in Figure A2(d), follows the same trend as the baseline case, with deviations of less than 0.5%, which can be attributed to the stochastic nature of the random walk model employed.

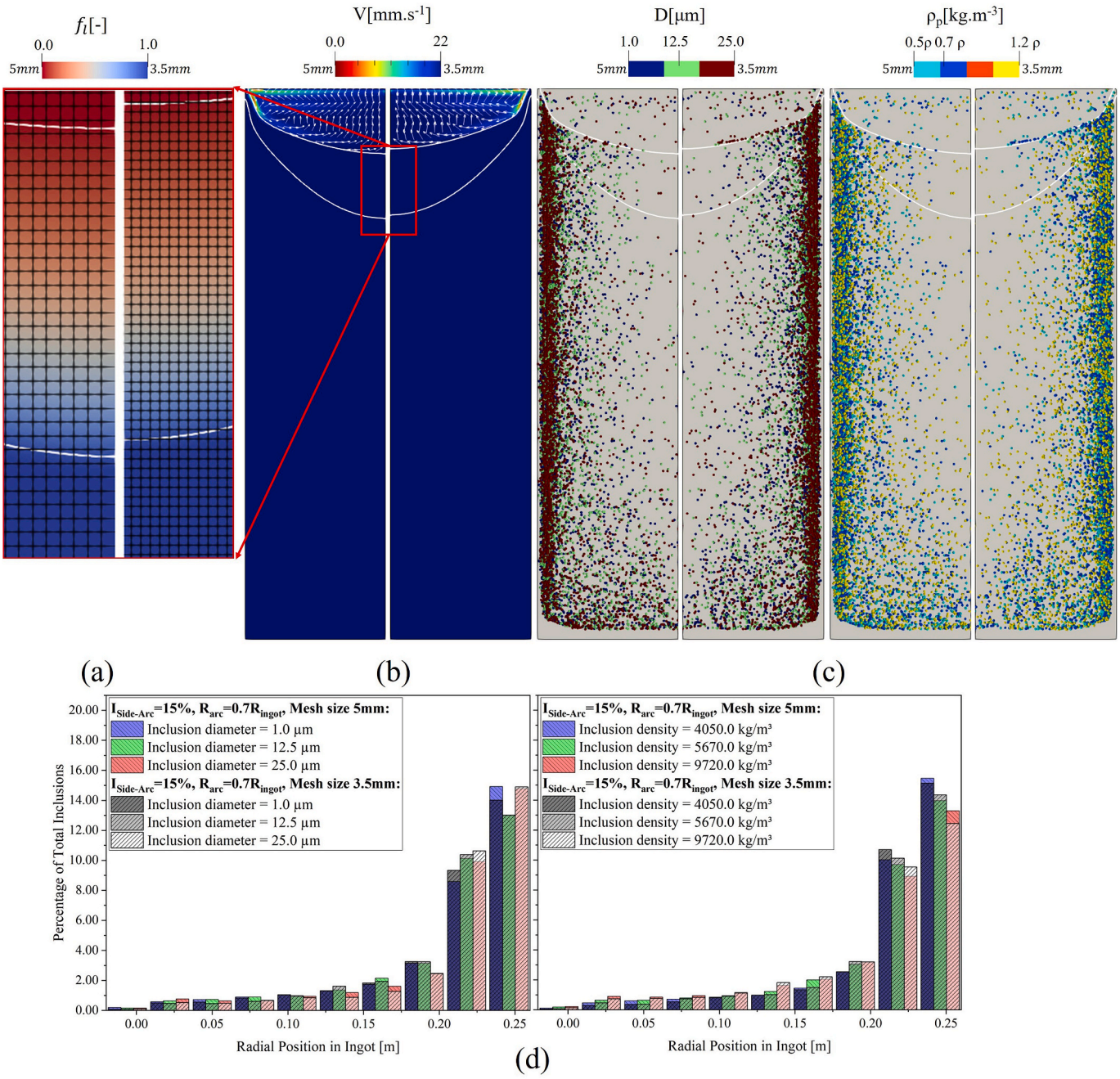

Fig. A2. Comparison of mesh sensitivity between the baseline mesh (5 mm) and a 30% finer mesh: (a) Liquid fraction contour with mesh distribution, zoomed-in view of the mushy zone, (b) velocity field in the melt pool, (c) inclusion distribution for different particle sizes and densities, and (d) statistical radial distribution of inclusions.

B. Influence of Marangoni Effect

To evaluate the influence of surface tension–driven flow, additional simulations were performed by incorporating the Marangoni effect into the model. The Marangoni stress was implemented at the melt surface based on the temperature-dependent surface tension gradient, expressed as: $\tau_{Mar} = \frac{d\gamma}{dT}\nabla T$, where $\frac{d\gamma}{dT}$ is the surface tension gradient with respect to temperature (see Table 3), and ∇T is the temperature gradient along the melt surface. All other modeling parameters and boundary conditions were kept identical to the baseline case to ensure a consistent comparison. The resulting flow behavior and inclusion transport characteristics were analyzed to assess the contribution of Marangoni-driven convection under the present conditions.

Figure A3 presents a comparison between simulations with and without the Marangoni effect. As assumed in the main model, the Marangoni effect is neglected. Figure A3(a) shows the velocity field in the melt pool for both cases, indicating a high degree of similarity in the flow structure. The melt-pool depth remains identical in both simulations.

Figure A3(b) illustrates the inclusion distribution, where similar patterns are observed, with only minor differences. These small variations are attributed to the stochastic nature of the random walk model rather than the influence of Marangoni forces. This is further supported by the statistical comparison in Figure A3(c), which shows nearly identical inclusion distributions in both magnitude and trend.

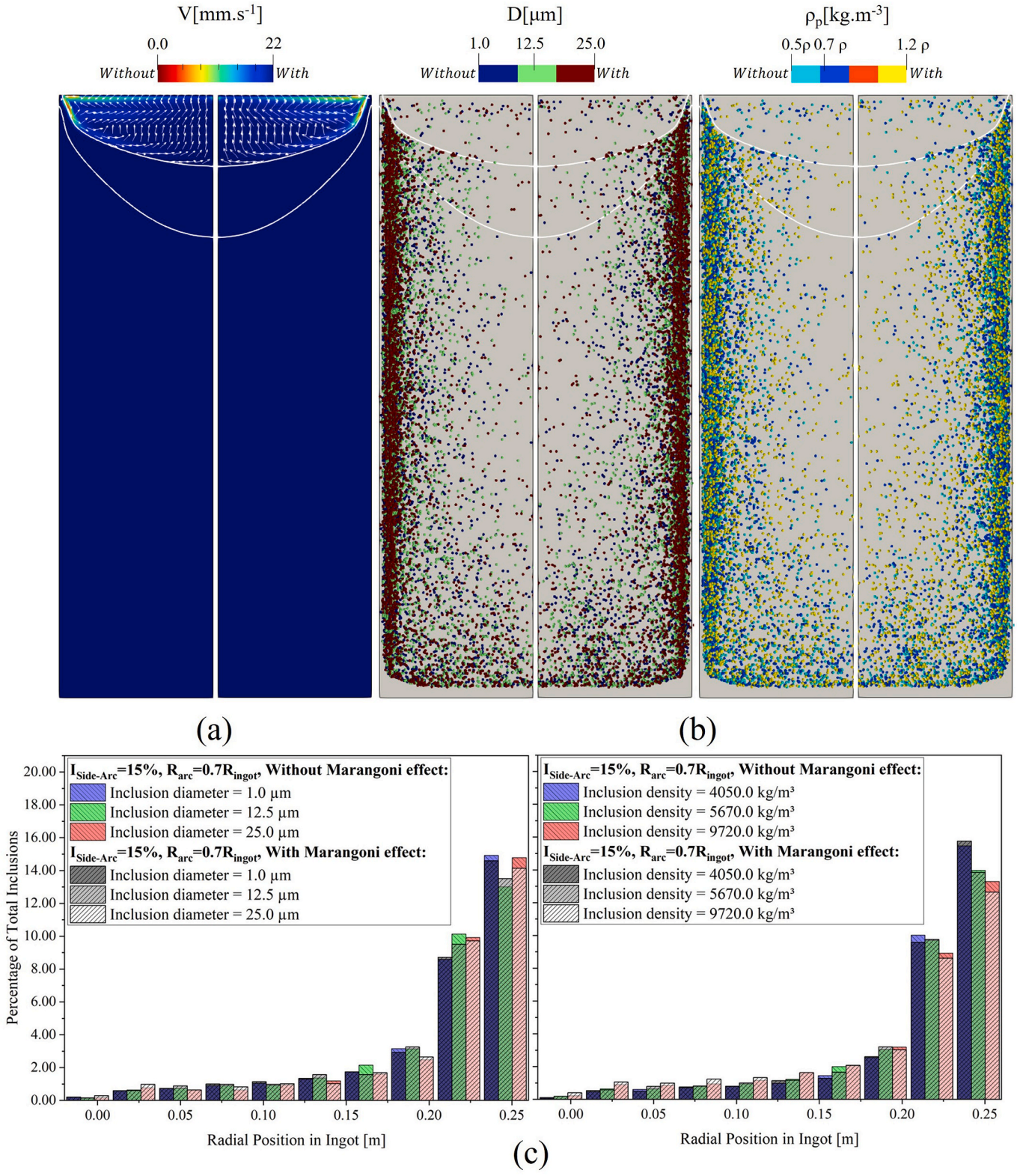

Fig. A3. Comparison of simulations with and without the Marangoni effect: (a) velocity field in the melt pool, (b) inclusion distribution for different particle sizes and densities, and (c) statistical radial distribution of inclusions.

C. Influence of Joule Heating

To evaluate the effect of Joule heating, additional simulations were performed in which volumetric resistive heating was included in the energy equation as a source term (J^2/σ_e). Joule heating arises from the dissipation of electrical energy due to the finite electrical resistance of the molten metal as current passes through the melt pool. Its magnitude depends on both the local current density and the electrical conductivity of the material.

In the present case, the alloy exhibits relatively high electrical conductivity, resulting in low electrical resistance and consequently limited volumetric heat generation. Furthermore, the majority of energy input in VAR is supplied by the arc and superheated droplets at the ingot surface, making Joule heating a secondary contribution to the overall thermal balance.

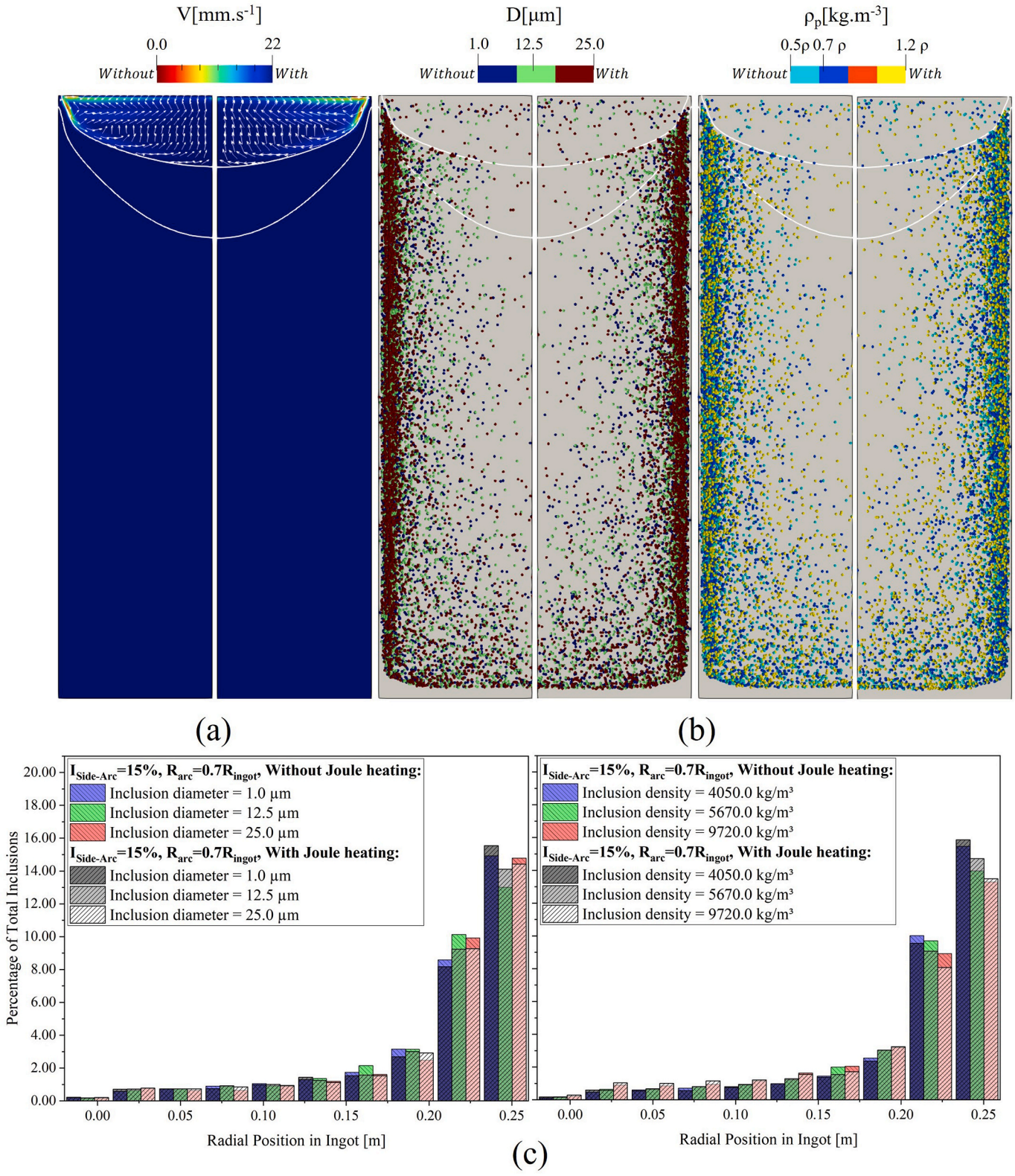

Fig. A4. Comparison of simulations with and without the Joule heating: (a) velocity field in the melt pool, (b) inclusion distribution for different particle sizes and densities, and (c) statistical radial distribution of inclusions.

All other model parameters and boundary conditions were kept identical to the baseline case to ensure a consistent comparison. The results indicate that the melt-pool profile and depth remain unchanged when Joule heating is considered (as shown in Figure A4(a)). The inclusion distribution also exhibits a similar pattern, with no noticeable differences in the overall trends (as shown in Figure A4(b)). Statistical analysis shows that the deviation in inclusion fraction is less than 1% near the ingot sidewall, and this difference gradually decreases toward the interior of the ingot, where the results become nearly identical (as shown in Figure A4(c)).

D. Effect of Inclusion Injection Points

In the VAR process, inclusions are introduced into the melt pool through multiple molten droplets falling from the electrode tip. In reality, this process is spatially distributed and highly dynamic, with inclusions entering the melt over a range of locations beneath the electrode. To represent this behavior in a computationally efficient manner, a limited number of discrete injection points is used to approximate the spatial distribution in a time-averaged sense.

In the baseline simulations, inclusions are introduced from five discrete locations beneath the electrode tip. To evaluate the influence of this assumption, an additional simulation was performed with an increased number of injection points (10 locations).

The resulting inclusion distribution contours, for both particle size and density, show behavior consistent with the baseline case (as shown in Figure A5(a)), with pronounced accumulation near the ingot sidewall and lower inclusion presence in the central region. The statistical distribution, presented in Figure A5(b), also follows an identical trend, with only minor discrepancies. These small differences are attributed to the stochastic nature of the random walk model used for particle tracking.

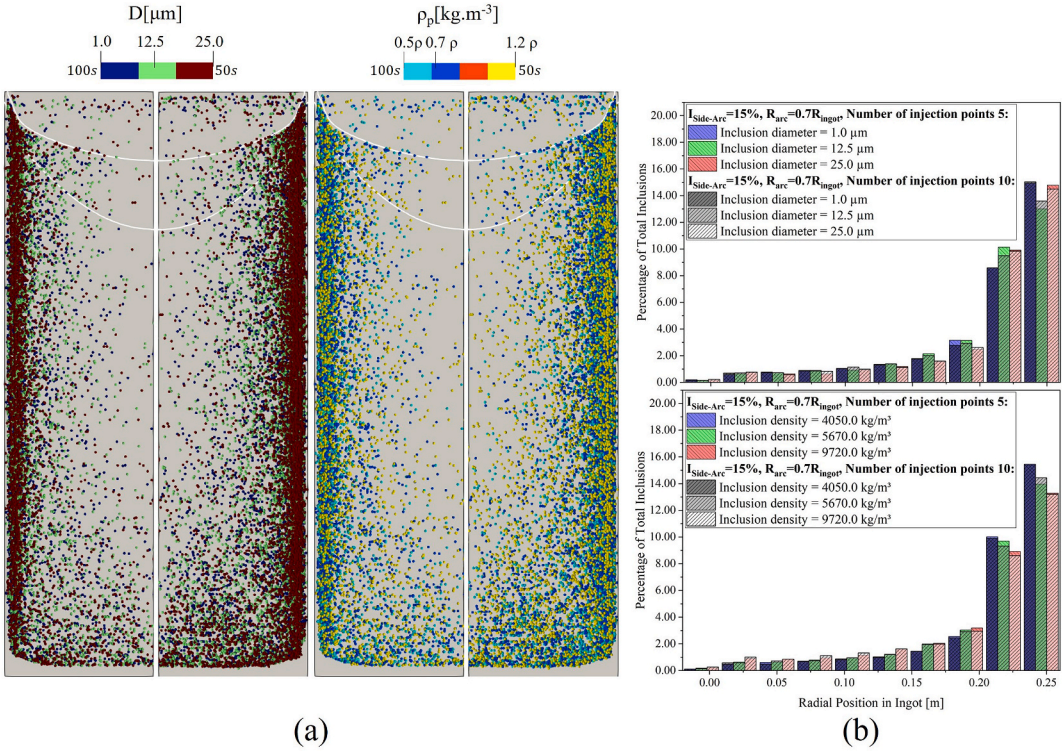

Fig. A5. (a) Effect of the number of inclusion injection points on distribution: (a) spatial distribution of inclusions for 5 and 10 injection locations, and (b) corresponding statistical distribution showing negligible differences between cases.

E. Effect of Injection Frequency

In the actual VAR process, droplet formation occurs continuously, with approximately 5–10 droplets generated per second for an industrial-scale VAR system with a 440 mm electrode remelted into a 510 mm ingot. Assuming that each droplet may carry inclusions with varying sizes and densities, a direct representation of this process would result in several million particles over the duration of the simulation. Modeling such a large number of inclusions would lead to prohibitively high computational costs, with simulation times extending to impractical levels.

Therefore, in the present study, a time-averaged injection approach is adopted, where inclusions are introduced at discrete intervals of 100 s. This approach provides a representative description of the overall inclusion transport and distribution within the ingot while maintaining computational efficiency. To assess the sensitivity of this assumption, an additional simulation was performed in which the injection frequency was increased, with inclusions introduced every 50 s. The resulting inclusion distribution across the entire ingot remains nearly identical to the baseline case (as shown in Figure A6 (a,b)). Both the spatial distribution and the statistical analysis show only minor differences, which can be attributed to the stochastic nature of the random walk model.

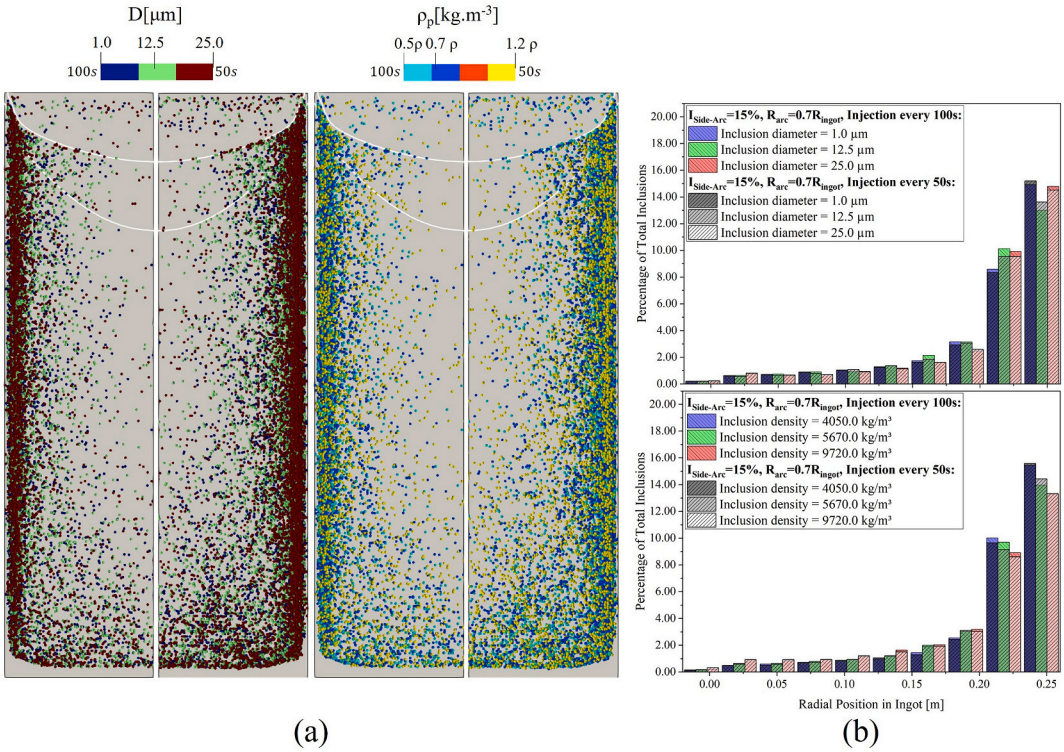

Fig. A6. Comparison of simulations of two different injection frequencies (every 50s and every 100s): (a) inclusion distribution for different particle sizes and densities, and (b) statistical radial distribution of inclusions.

F. Effect of Inclusion Entrapment Criterion

The entrapment of inclusions during solidification is governed by the interaction between the advancing solid–liquid interface and particle motion within the mushy zone. In reality, inclusion capture is strongly influenced by local solidification conditions, interdendritic flow, and solute redistribution, which affect dendrite morphology and permeability. A fully accurate description of inclusion entrapment would therefore require coupling with solute transport and microsegregation models to resolve the evolution of the dendritic structure and local composition. However, such an approach is beyond the scope of the present study.

Instead, inclusion entrapment is approximated using a liquid fraction–based criterion, which is consistent with the macroscopic solidification model employed. In this approach, particles are considered captured once they enter regions where the liquid fraction falls below a specified threshold, effectively representing the reduced permeability and mobility within the mushy zone. In the present study, a threshold of $f_l<0.9$ is used to define inclusion entrapment. While higher thresholds (e.g., $f_l<0.95$) have been reported in the literature for steel alloys (lab scale VAR), nickel-based alloys typically exhibit larger primary dendrite arm spacing, allowing inclusions to penetrate deeper into the mushy zone before being captured. Therefore, a threshold of 0.9 is considered more appropriate for the present alloy system. To assess the sensitivity of this assumption, an additional simulation was performed using a higher entrapment criterion of $f_l<0.95$. As shown in Figure A7(a), the mushy zone near the ingot sidewall is relatively narrow, with smaller dendrite spacing and a steep temperature gradient. In this region, the melt flow velocity is highest, directed from the center toward the ingot wall, resulting in a dominant drag force acting on the inclusions. Under these conditions, the difference between the two entrapment criteria ($f_l<0.0$ and $f_l<0.95$) becomes negligible, as both thresholds correspond to closely located regions within the mushy zone. Consequently, only minor differences in inclusion capture are observed near the ingot wall. Toward the bottom of the melt pool, although the difference in liquid fraction between these thresholds becomes larger, the local flow velocity is significantly reduced. As a result, the drag force is insufficient to transport inclusions into deeper regions, leading to minimal differences in inclusion entrapment. This behavior is also reflected in the statistical distribution (Figure A7(b,c)), where only negligible variations are observed between the two cases.

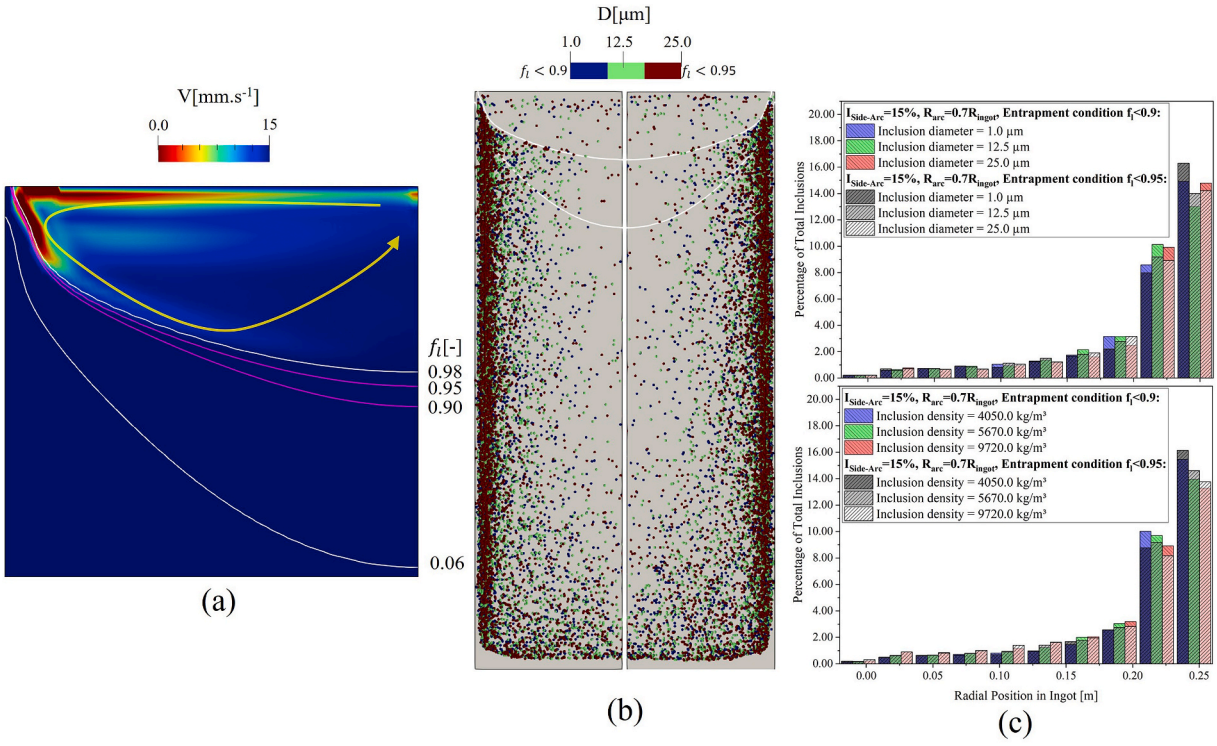

Fig. A7. (a) velocity field in the melt pool, (b) inclusion distribution for different particle sizes, and (c) statistical radial distribution of inclusions.

E. Comparison between Thermal Buoyancy Flow and Electro-Vortex Flow

In the melt pool of the ingot, two primary flow mechanisms are present: electro-vortex flow (EVF) and thermal buoyancy flow (TBF). The electro-vortex flow arises from the interaction between the electric current and the magnetic field, while thermal buoyancy flow is driven by density variations due to temperature gradients (thermal expansion). The dominance of each mechanism depends on their relative strength. For the present alloy system, thermal expansion is significant; therefore, under diffusive arc conditions, the flow is primarily governed by thermal buoyancy, resulting in a single counterclockwise circulation within the melt pool. As the arc becomes more constricted, the current density becomes more localized and stronger, leading to the emergence of electro-vortex flow. This introduces a clockwise circulation and inward-directed flow toward the center of the ingot. Figure A8 illustrates the comparison between these two driving forces. Under diffusive arc conditions, the thermal buoyancy force is significantly stronger than the Lorentz force. With increasing side arcing, the Lorentz force becomes weaker due to the redistribution of current. In contrast, for constricted arc conditions, the Lorentz force intensifies and extends throughout the melt pool, while the thermal buoyancy force becomes more localized near the center. This interaction leads to the formation of an additional vortex structure, as observed in the velocity contours.

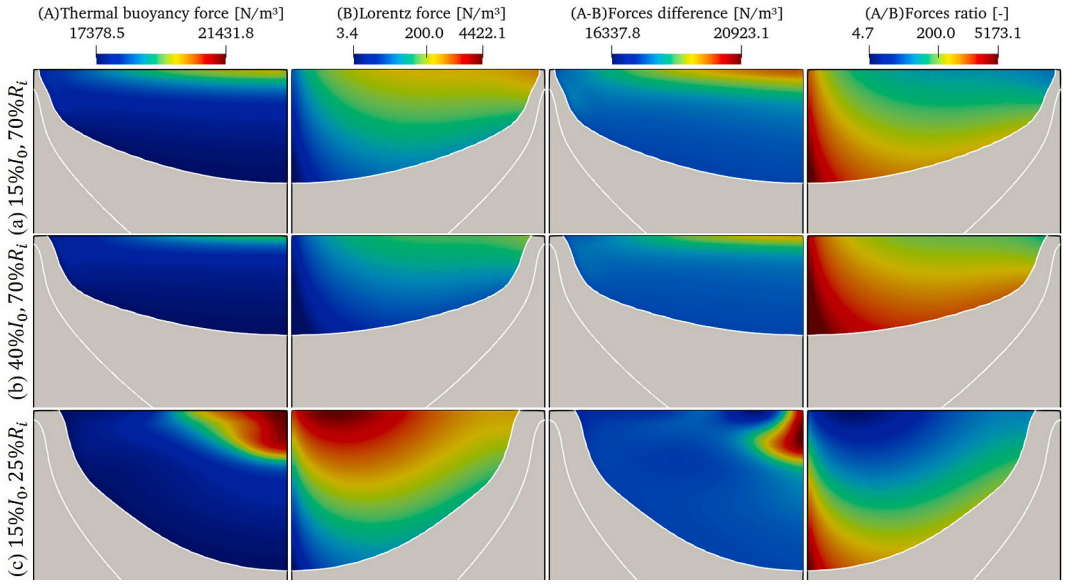

Fig. A8. Comparison of thermal buoyancy force and Lorentz force under different arc conditions, illustrating their relative strength and distribution within the melt pool. Each row indicates the condition of side arcing and arc distribution.

F. Analysis of Forces Acting on Inclusions and Particle Trajectories

In the present model, several forces acting on inclusions are considered, including drag force, pressure gradient force, virtual mass force, Saffman lift force, buoyancy (gravity) force, and additional body forces arising from the flow field. The relative magnitude of these forces is evaluated and presented in Figure A9.

Figure A9(a) shows a representative snapshot at $t = 100$, illustrating the spatial distribution and magnitude of the forces acting on the inclusions. It can be observed that inclusions are predominantly entrained within a vortex structure driven by the outward thermal buoyancy flow, which is the dominant flow mechanism under the present condition (side-arcing intensity of 15% and an arc ratio of 70% (diffusive arc)). As a result, a large fraction of inclusions is transported toward the ingot sidewall and accumulates beneath this vortex structure in solidified ingot.

The particle trajectories are shown in Figure A9(b), demonstrating that once inclusions enter the melt pool, they are rapidly driven outward by thermal buoyancy flow and subsequently follow recirculating paths within the vortex before being captured in the mushy zone. The streamline representation also indicates the particle Reynolds number along the trajectories, while the particle color denotes relative density.

A quantitative comparison of the acting forces (Figure A9(c)) shows that the drag force is the dominant force governing particle motion, primarily due to the strong outward flow induced by thermal buoyancy. The next most significant contributions arise from gravity and buoyancy forces, followed by the pressure gradient force. In contrast, the virtual mass force and Saffman lift force are considerably smaller in comparison.

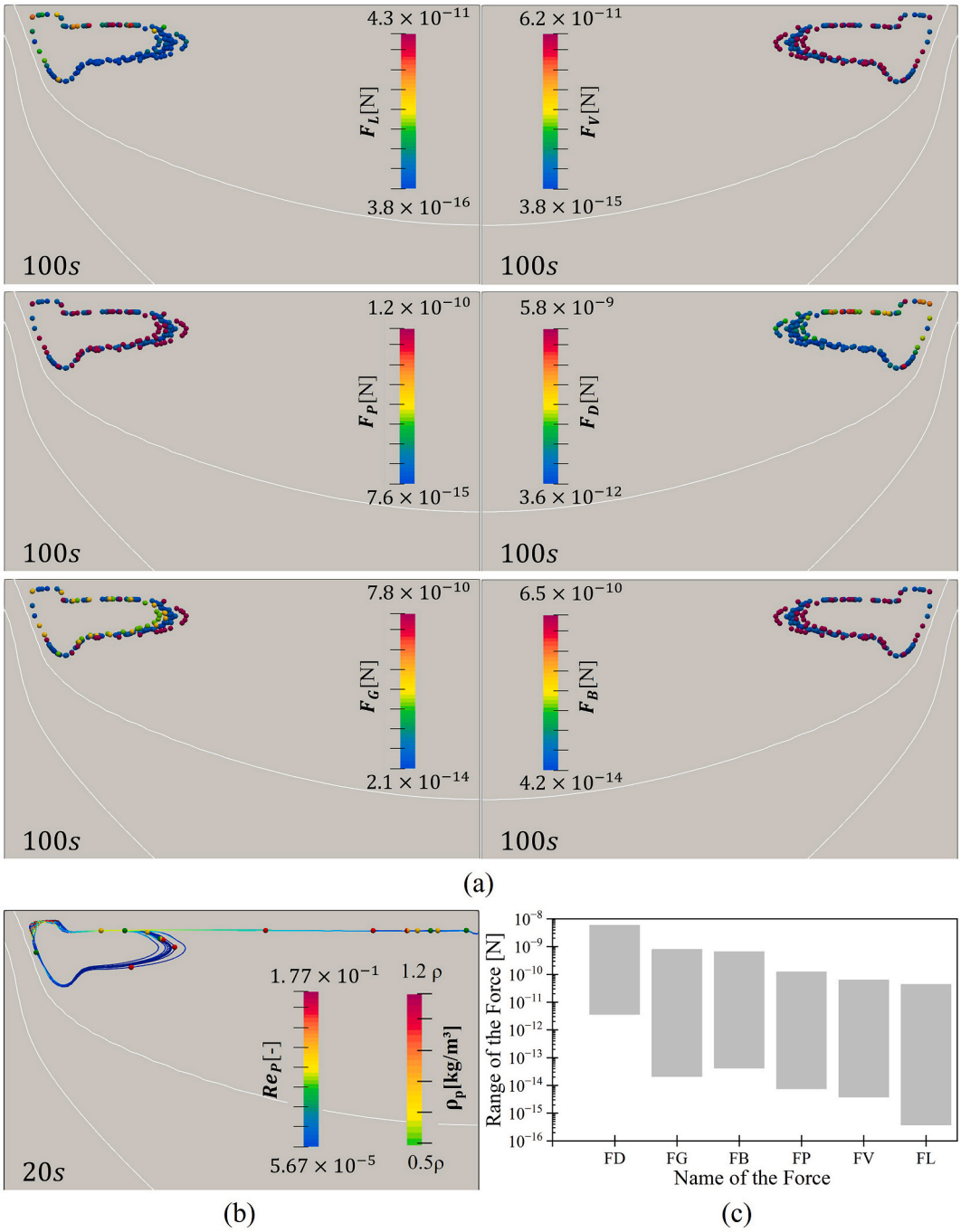

Fig. A9. Analysis of forces acting on inclusions and their trajectories: (a) spatial distribution and magnitude of forces, (b) particle trajectories colored by density with Reynolds number indication, and (c) quantitative comparison of force magnitudes.

References

[1] Abdi M, Karimi-Sibaki E, Sommitsch C, Barati H, Al-Nasser M, Wu M, Teplyakov I, Kharicha A. Int J Thermofluids 2024;23:100721.
[2] Mitchell A. Materials Science and Engineering: A 2005;413–414:10–8.
[3] Bertram L. Modeling for casting and solidification processing. Madison Avenue, New York, NY 10016, USA: Marcel Dekker, Inc; 2002. p. 565–612. 2002.
[4] G. Jarczyk and H. Franz: Archives of materials science and engineering.
[5] Tomasello C, Shannon G. In: *Bearing steel technologies: 12th volume, progress in bearing steel metallurgical testing and quality assurance*, ASTM International 100 Barr harbor drive. West Conshohocken, PA: PO Box C700; 2020. p. 515–27. 19428-2959.
[6] Zanner FJ, Williamson RL, Harrison RP, Flanders HD, Thompson RD, Szeto WC. In: Superalloys 718 metallurgy and applications. TMS; 1989. p. 17–32. 1989.
[7] Zababluev YuI, Buryakovskii GA. Metallurgist 1984;28:19–21.
[8] Arreola-Herrera R, Cruz-Ramírez A, Rivera-Salinas JE, Romero-Serrano JA, Sánchez-Alvarado RG. Theor Appl Fract Mech 2018;94:134–46.
[9] Chen Z, Yang S, Qu J, Li J, Dong A, Gu Y. Materials 2018;11:1838.
[10] Holappa L, Wijk O. In: Treatise on process metallurgy. Elsevier; 2014. p. 347–72.
[11] Yang S, Zhao P, Yang S, Liu W, Li J, Zheng L. Metall Mater Trans B 2022;53:760–9.
[12] Grignard JF, Soller A, Jourdan J, Bellot J, Jardy A. Adv Eng Mater 2011;13:563–9.
[13] Descotes V, Quatravaux T, Bellot J-P, Witzke S, Jardy A. Metals 2020;10:541.
[14] Kobernik NV, Galinovskii AL, Pankratov AS, Aleksandrova VV, Andriyanov YuV, Orlik AG. Russ Metall 2023;2023:657–64.
[15] Mitchell A. High Temp Mater Process 2005;24:101–10.
[16] Song Y, Zhang H, Ren L. Eng Rep 2024;6:e12892.
[17] Zhao P, Gu Y, Yang S, Liu W, Li J, Du J. Metall Mater Trans B 2023;54:698–711.
[18] Rungta R, Skidmore AJ, Buchhei RD. In: Proceedings of a Sympo-sium held in conjunction with the world materials congress. ASM International; 1988. p. 1–19.

[19] Yang S, Yang S, Qu J, Du J, Gu Y, Zhao P, Wang N. J Iron Steel Res Int 2021;28:921–37.
[20] Zhang W, Lee PD, McLean M, Siddall RJ. In: Superalloys 2000 (ninth international symposium). TMS; 2000. p. 29–37.
[21] Carnegie Mellon University, A. Huck, B. Webler, and Carnegie Mellon University: I&ST, DOI:10.33313/TR/0724.1.
[22] Ghazal G, Jardy A, Chapelle P, Millet Y. Metall Mater Trans B 2010;41:646–59.
[23] Cen M, Liu Y, Chen X, Zhang H, Li Y. China Foundry 2019;16:223–31.
[24] Pericleous K, Djambazov G, Ward M, Yuan L, Lee PD. Metall Mater Trans A 2013;44:5365–76.
[25] E. Samuelsson: DOI:10.14288/1.0078542.
[26] M. Abdi, E. Karimi-Sibaki, M. Wu, and A. Kharicha: Metall Mater Trans B, DOI: 10.1007/s11663-025-03749-8.
[27] Karimi-Sibaki E, Kharicha A, Vakhrushev A, Abdi M, Wu M, Ludwig A, Bohacek J, Preiss B. J Mater Res Technol 2022;19:183–93.
[28] Beilis IsakI. IEEE Trans Plasma Sci 2019;47:3412–33.
[29] Lafferty JM. In: Encyclopedia of physical science and technology. Elsevier; 2003. p. 359–70.
[30] Juttner B. IEEE Trans Plasma Sci 1987;15:474–80.
[31] Anders A, Anders S, Jüttner B, Pursch H, Bötticher W, Lück H. J Appl Phys 1992;71:4763–70.
[32] Anders A. Cathodic arcs: from fractal spots to energetic condensation. New York: Springer; 2008.
[33] Tezenas Du Montcel B, Chapelle P, Creusot C, Jardy A. IEEE Trans Plasma Sci 2018;46:3722–30.
[34] Karimi-Sibaki E, Kharicha A, Abdi M, Vakhrushev A, Wu M, Ludwig A, Bohacek J. Metall Mater Trans B 2021;52:3354–62.
[35] Boxman RL, Sanders DM, Martin PJ, editors. Handbook of vacuum Arc science and technology: fundamentals and applications. Park Ridge, N.J., U.S.A: Noyes Publications; 1995.
[36] Cui J, Li B, Liu Z, Qi F, Xu J, Zhang J. J Mater Res Technol 2022;18:3991–4006.
[37] Chaly AM, Logatchev AA, Shkol'nik SM. IEEE Trans Plasma Sci 1997;25:564–70.
[38] Zalucki Z, Janiszewski J. IEEE Trans Plasma Sci 1999;27:991–1000.
[39] Zhang Z, Dorari E, Minisandram R, Krishnamoorthi S, Yuan L. J Mater Res Technol 2026;41:3492–506.
[40] Karimi-Sibaki E, Kharicha A, Wu M, Ludwig A, Bohacek J. Metall Mater Trans B 2020;51:222–35.
[41] Williamson RL, Shelmidine GJ, Maroone JP. *Report number: SAND2005-2838C*, research org. Albuquerque, NM, and Livermore, CA (United States): Sandia National Laboratories (SNL); 2005.
[42] Risacher A, Chapelle P, Jardy A, Escaffre J, Poisson H. J Mater Process Technol 2013;213:291–9.
[43] Bohacek J, Karimi-Sibaki E, Vakhrushev A, Mraz K, Hvozda J, Wu M, Kharicha A. Metall Mater Trans B 2024;55:4408–17.
[44] Woodside CR, King PE, Nordlund C. Metall Mater Trans B 2013;44:154–65.
[45] Zhang W, Lee PD, McLean M. Metall Mater Trans A 2002;33:443–54.
[46] Mitchell A. Ironmak Steelmak 2021;48:505–13.
[47] Pericleous KA, Bojarevics V, Djambazov GS. In: Eskin DG, Mi J, editors. Solidification processing of metallic alloys under external fields. Cham: Springer International Publishing; 2018. p. 75–118.
[48] Shamblen CE, Chang DR, Corrado JA. In: Superalloys 1984 (fifth international symposium). TMS; 1984. p. 509–20.
[49] Stefanescu DM. Science and engineering of casting solidification. Cham: Springer International Publishing; 2015.
[50] Adolfi S. *Slag inclusion formation during solidification of steel alloys and in cast iron*, materialvetenskap. Stockholm: Kungliga Tekniska högskolan; 2007.
[51] Shamsuddin M. In: Physical chemistry of metallurgical processes. second ed. Cham: Springer International Publishing; 2021. p. 389–427.
[52] Jiang D, Ren Y, Zhang L. JOM 2024;76:3362–71.
[53] Wang X, Ward RM, Jacobs MH, Barratt MD. Metall Mater Trans A 2008;39:2981–9.
[54] Shi X, Duan S-C, Yang W-S, Mao M-T, Guo H-J, Guo J. Metall Mater Trans B 2019;50:3072–87.
[55] Mitchell A. Materials technology, vol. 9; 1994. p. 201–6.
[56] Mitchell A, Reed RC. High Temp Mater Process 2009;28:285–98.
[57] Zhang L, Thomas BG. ISIJ Int 2003;43:271–91.
[58] Walkner C, Mukhametzianova G, Wagner S, Korp JC, Graf A, Irrgeher J, Meisel TC, Prohaska T. Metals 2025;15:67.
[59] Zhang W, Lee PD, McLean M. In: Morris DG, Naka S, Caron P, editors. Intermetallics and superalloys. first ed. Wiley; 2000. p. 121–8.
[60] Van Den Avyle JA, Brooks JA, Powell AC. JOM 1998;50:22–5.
[61] Dreshfield RL. JOM 1987;39:16–21.
[62] Gao J, Zhu H, Li H, Ni Z, He Z, Jiang Z, Zhang S, Feng H. Steel research int. 2025, 2500064.
[63] Jiang D, Ren Y, Zhang L. Metall Mater Trans B 2023;54:1342–51.
[64] Pan T, Zhu H, Jiang Z, Li H, Liu F, Zhang R, He Z, Ni Z. steel research int 2024;95:2300649.
[65] Davidson PA, Thess A, editors. Magnetohydrodynamics. Vienna: Springer Vienna; 2002.
[66] Zagrebelnyy D, Krane MJM. Metall Mater Trans B 2009;40:281–8.
[67] Lee PD, Lothian R, Hobbs LJ, McLean M. In: Superalloys 1996 (eighth international symposium). TMS; 1996. p. 435–42.
[68] Beaman JJ, Felipe Lopez L, Williamson RL. Journal of dynamic systems, measurement, and control, vol. 136; 2014, 031007.
[69] Carman PC. Chem Eng Res Des 1997;75:S32–48.
[70] A. Vakhrushev and M. Wu: .
[71] Menter FR. AIAA J 1994;32:1598–605.
[72] E.N. Kondrashov, M.I. Musatov, A.Yu Maksimov, A.E. Goncharov, and L.V. Konovalov: 2005.
[73] Lee PD, Quested PN, McLean M. Philos Trans R Soc London, Ser A: Math Phys Eng Sci 1998;356:1027–43.
[74] Yang S, Tian Q, Yu P, Yang S, Liu W, Li J. J Mater Res Technol 2023;24:2828–38.
[75] Xiong Y, Liu Z, Zhao Z, Li B. Metall Mater Trans B 2024;55:4182–99.
[76] L.G. Hosamani: Oregon Health & Science University, 1988.
[77] Cibula M, King P, Motley J. Metall Mater Trans B 2020;51:2483–91.
[78] Nair BG, Winter N, Daniel B, Ward RM. IOP Conf Ser Mater Sci Eng 2016;143:012012.
[79] Karimi-Sibaki E, Peyha M, Vakhrushev A, Wu M, Ludwig A, Bohacek J, Preiss B, Kharicha A. Sci Rep 2022;12:20405.
[80] Williamson RL, Shelmidine GJ. In: Superalloys 718, 625, 706 and various derivatives. TMS; 2001. p. 91–102. 2001.
[81] Ward RM, Jacobs MH. J Mater Sci 2004;39:7135–43.
[82] Chapelle P, Ward RM, Jardy A, Weber V, Bellot JP, Minvielle M. Metall Mater Trans B 2009;40:254–62.
[83] Bhar R, Jardy A, Chapelle P, Descotes V. Metall Mater Trans B 2020;51:2492–503.
[84] Ludwig A, Shayesteh G, Stefan-Kharicha M, Wu M, Kharicha A. Int J Heat Mass Tran 2025;240:126638.
[85] Wu M, Ludwig A. Acta Mater 2009;57:5632–44.
[86] Wu M, Ludwig A, Kharicha A. Metals 2019;9:229.